Towards balancing the oceanic Ni budget

S.H. Little[1,2], C. Archer[3], J. McManus[4], J. Najorka[5], A. V. Wegorzewski[6], D. Vance[3]

1. Department of Earth Sciences, University College London, Gower Place, London WC1E 6BS, UK.
2. Department of Earth Science and Engineering, Royal School of Mines, Imperial College London, London, SW7 2BP, UK.
3. Institute of Geochemistry and Petrology, Department of Earth Sciences, ETH Zürich, Clausiusstrasse 25, 8092 Zürich, Switzerland.
4. Bigelow Laboratory for Ocean Sciences, 60 Bigelow Drive, P.O. Box 380, East Boothbay, Maine 04544, USA.
5. Core Research Laboratories, The Natural History Museum, Cromwell Road, London SW7 5BD, UK.
6. Federal Institute for Geosciences and Natural Resources (BGR), Stilleweg 2, D-30655 Hannover, Germany.

Corresponding author: susan.little@ucl.ac.uk

For resubmission to: EPSL

3 June 2020

Abstract

Nickel isotopes are a novel and promising tracer of the chemistry of past ocean environments, but realisation of this tracer's potential requires a comprehensive understanding of the controls on Ni burial in the marine sedimentary archive. An outstanding puzzle in the marine budget of Ni, first recognised in the 1970s, is a major imbalance in the known inputs and outputs to and from the ocean: the sedimentary outputs of Ni are much larger than the inputs (rivers, dust). Much more recently, it has also been recognised that the outputs are also considerably isotopically heavier than the inputs. In this study, we find light Ni isotope compositions ($\delta^{60}\mathrm{Ni}_{\mathrm{NIST\ SRM986}}$ = –0.2 to –0.8‰) for Mn-rich sediments from the eastern Pacific compared to Fe-Mn crusts (at about +1.6‰). These data suggest that diagenetic remobilisation of isotopically heavy Ni leads to a significant benthic Ni flux (estimated at $0.6 – 2.3 \times 10^8$ mol/yr), similar in magnitude to the riverine flux, to the ocean. Diagenetic remobilisation of Ni may occur either via cycles of Mn-oxide dissolution and precipitation, with associated Ni sorption and release, or during mineralogical transformation of birnessite to todorokite. A minor role for retention of isotopically light Ni by Fe oxides or Fe-rich authigenic clays is also proposed. Overall, a benthic flux of isotopically heavy Ni (at about +3‰) can balance the marine Ni budget, pinpointing diagenesis as a key missing piece of the Ni puzzle.

1. Introduction

Nickel is a cofactor in several enzyme systems central to the production of gases (CO_2, CO, methane, ammonia, O_2, H_2) that are important to the carbon, nitrogen and oxygen cycles (reviewed by Ragsdale, 2009). Nickel is utilised by marine phytoplankton as the metal centre in urease, which catalyses the breakdown of urea to NH_3 and CO_2 (e.g., Price and Morel, 1991). A Ni-containing superoxide dismutase (Ni-SOD) enzyme is also present in some marine plankton groups, used to detoxify reactive oxygen species (e.g., Palenik et al., 2003). All methanogens have an obligate Ni requirement due to the presence of several Ni containing enzymes, including methyl-coenzyme M reductase (e.g., Jaun and Thauer, 2007). Methane may have played a key role in maintaining a warm climate on the early Earth, leading to interest in the development of Ni and its isotopes as a biomarker for methanogenesis (e.g., Cameron et al., 2009; Wang et al., 2019).

The stable isotopes of Ni (reported as $\delta^{60/58}Ni = (^{60}Ni/^{58}Ni_{sample}/^{60}Ni/^{58}Ni_{SRM986} - 1) \times 1000$) could help to quantify and understand these issues in the past. However, the development of a new isotope system as a tracer requires characterization of its modern biogeochemical cycling. Indeed, stable isotope ratios provide useful constraints on elemental global mass balances; that is, the input and output fluxes of an element to and from the ocean. If we assume steady state, the Ni input and output fluxes should balance (equation 1), as should their flux-weighted isotopic compositions (equation 2):

(1) $F_{input} = F_{output}$

(2) $F_{input}\delta_{input} = F_{output}\delta_{output}$

where F_{input} and F_{output} are the respective input and output flux magnitudes, and δ_{input} and δ_{output} their isotopic compositions. For our discussion here we assume that Ni is at steady state over the past 10 – 20 kyr, i.e., on the timescale of the oceanic residence time of Ni (Ciscato et al., 2018 this study).

Current best estimates of the inputs and outputs of Ni to and from the oceanic dissolved pool are not in balance (Krishnaswami, 1976; Gall et al., 2013; Cameron and Vance, 2014; Gueguen et al., 2016; Ciscato et al., 2018; Spivak-Birndorf et al., 2018). The estimated total input of Ni to the ocean is approximately half of the total sedimentary output fluxes. In addition, the known inputs are isotopically light (at about +0.8‰; Cameron and Vance, 2014) compared to seawater (at about +1.4‰; Archer et al., 2020; Cameron and Vance, 2014; Takano et al., 2017; Wang et al., 2018), while most of the sedimentary outputs are isotopically similar to or heavier than seawater (Gall et al., 2013; Gueguen et al., 2016; Ciscato et al., 2018). Balancing the steady-state Ni budget either requires an isotopically heavy Ni input or an isotopically light output flux, or both of these.

One key oceanic output flux of Ni is sorption to dispersed Fe-Mn oxide phases found throughout oxygenated deep sea sediments, for which the isotopic composition of Fe-Mn crusts has been used as a proxy (Cameron and Vance, 2014; Ciscato et al., 2018). The Ni isotope composition of Fe-Mn crusts is variable, but generally similar to or heavier than seawater, with average $\delta^{60}Ni_{Fe\text{-}Mn\ crust} = +1.62 \pm 0.37‰$ (n = 28; 1 SD, Gall et al., 2013; Gueguen et al., 2016). Nickel is sorbed to the Mn oxide phase in Fe-Mn crusts: specifically, to a poorly crystalline phyllomanganate of the birnessite family (termed vernadite/δ-MnO_2) (e.g., Koschinsky and Halbach, 1995; Koschinsky and Hein, 2003; Peacock and Sherman, 2007a). However, sediments and Mn nodules contain a mixture of vernadite and more crystalline 7Å and 10Å birnessite phases, which transform to the tectomanganate phase todorokite during diagenesis (e.g., Burns and Burns, 1979; Atkins et al., 2014). Recent experiments and the study of todorokite-rich buried Mn nodules have shown that ~50% of sorbed Ni is released to the aqueous phase during this mineralogical transformation (Atkins et al., 2016; Heller et al., 2018). In addition, remobilization of Ni is observed in the Mn oxide reduction zone in sub-oxic sediment porewaters (e.g., Klinkhammer, 1980; Heggie et al., 1986), where 'sub-oxic' denotes low concentrations of both oxygen and sulphide. Either transformation to todorokite or the reduction of Mn oxides may lead to a decreased Ni trapping efficiency in sediments and a benthic return flux of Ni to seawater.

As yet, the potential for isotope fractionation during diagenetic Ni remobilization has not been evaluated. We show that diagenesis significantly modifies the output flux of Ni from the oceans, and infer a benthic return flux of isotopically heavy Ni. We explore the extent to which this benthic flux can balance the oceanic Ni budget.

2. Sites and Samples

Metalliferous sediment samples were selected from two of the five MANOP (Manganese nodule project) sites, M and H, both in the Guatemala Basin (Fig. 1). Both sites are oxygenated at the sediment-water interface and sub-oxic below (Klinkhammer, 1980). A surface nitrate maximum overlies a zone of Mn cycling, with detectable porewater Mn at depths > 6 cm at Site M, and > 12 cm at Site H. Porewater Fe is observed at depths > 13 cm at site M only (Fig. 3; Klinkhammer, 1980; Heggie et al., 1986). Samples were collected using a 50 cm x 50 cm box corer and later sub-sampled with a plastic core liner, using a piston to avoid core shortening. Five-six sub-samples from the upper 20 cm of each core were included in this study.

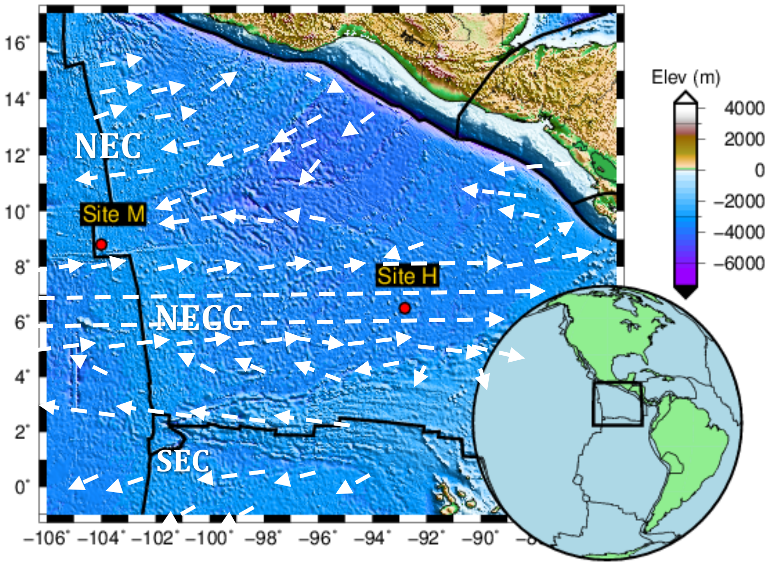

Figure 1. Map of the Guatemala Basin showing the two MANOP site locations. Site M is close to the East Pacific Rise, Site H is located on the flat plain of the Guatemala Basin. Tectonic plate boundaries in black; surface ocean currents as white arrows (NECC, North Equatorial Counter Current; NEC, North Equatorial Current; SEC, South Equatorial Current) from Kessler (2006). Insert shows the location of the grid.

MANOP site M, chosen by MANOP to represent hydrothermal sedimentation, is located 25 km east of the spreading axis of the East Pacific Rise, at 8.8°N 104.0° W, ~3.1 km water depth (Fig. 1). The site is just 1,000 km away from the Central American coast and within the source region of the westward flowing North Equatorial Current (NEC). As a result, site M has a sedimentation rate of about 1 cm/1000 year (Kadko, 1981), with a combination of continental, hydrothermally-derived, and biogenic sediment (at ~130 µg C_{org}/cm^2yr; Lyle et al., 1984). Surface sediments at site M contain 10–40% calcium carbonate, 5–9% opal, and 1–2% organic carbon (Lyle et al., 1984).

MANOP site H, the hemipelagic MANOP site, is located approximately 1,000 km east of the East Pacific Rise on a relatively flat plain in the Guatemala Basin, at 6.5°N 92.8°W, ~3.6 km water depth. It lies at the northern edge of the eastward flowing North Equatorial Counter-Current (NECC) and at the southwestern edge of the productive Costa Rica Dome. The organic C flux at this site is similar to that at site M, at ~110 µg C_{org}/cm^2yr (Lyle et al., 1984). The site is currently at or just below the calcite compensation depth, and the sedimentation rate, at ~0.65 cm/1000 yr, is about half of that of site M due to greater dissolution of biogenic debris (carbonate) and the lower quantity of continent-derived material (Kadko, 1981; Lyle et al., 1984).

Bulk samples of six well-characterized Mn nodule samples were also analysed for their Ni isotope compositions in this study (Table 1). These include the two USGS reference materials Nod P1 and Nod A1, one surface and two buried Fe-Mn nodules from the Clarion-Clipperton Zone (CCZ) of the equatorial North Pacific (sites 21KG, 22KL; full details in: Heller et al., 2018; Wegorzewski et al., 2020) and one shallow buried nodule from the Peru Basin (site 77BC). The selected surface and buried nodules have evolved under differing redox regimes and are therefore compositionally diverse, allowing comparisons to be made between phyllomanganate-rich and todorokite-rich nodules (Table 1; Wegorzewski et al., 2020).

Table 1. Mn nodule samples studied, with predominant mineralogy as determined by XRD analysis (Wegorzewski et al., 2020)

Mn Nodule	Location	Water depth/ Depth in sediment	Mineralogy
Nod A1	Atlantic 31°02’N 78°22’W	788 m / Surface	Phyllomanganates
Nod P1	Pacific 14°50’N 124°28’W	4300 m / Surface	Phyllomanganates

21KG-1n	CCZ, Pacific 13°10.529’N 118°08.187’W	4288 m/ Surface	Diagenetic growth structures: 7 and 10 Å phyllomanganates and hydrogenetic growth structures: vernadite (δ-MnO$_2$) that is epitaxially intergrown with an amorphous FeOOH phase
77BC11-6	Peru Basin, Pacific 7°04.575’ S 88°31.577’ W	4130.5 m/ Shallowly buried	Mainly Todorokite
22KL-530cm	CCZ, Pacific 13°10.527’N 118°08.184’W	4302 m/ Deeply buried 530 cm	Mainly Todorokite, minor phyllomanganates
22KL-801cm	CCZ, Pacific 13°10.527’N 118°08.184’W	4302 m/ Deeply buried 801 cm	Mainly Todorokite, minor phyllomanganates

3. Analytical Methods

3.1 MANOP mineralogy by XRD

Selected samples from MANOP sites H and M (Table 2) were analysed by X-ray diffractometry for their bulk mineralogy using a PANalytical X’Pert PRO instrument at the Natural History Museum, London. Phase quantification was subsequently attempted via a Rietveld refinement analysis of the 10 – 90° 2θ region. Note that the detection limit for the XRD analyses corresponds to about 1 – 5 wt%, depending on the crystallinity and crystal symmetry of the phase (where a higher crystallinity and crystal symmetry of a phase corresponds to a lower detection limit). For full details of the XRD analyses, see the Supplementary Information.

3.2 Element concentrations and Ni isotope ratios

Bulk sample digestion was carried out in clean laboratories at ETH Zürich or Imperial College London, following previously published methods (Cameron and Vance, 2014; Vance et al., 2016; Ciscato et al., 2018; Archer et al., 2020). Between 20 and 100 mg of each sample was pre-digested by treatment with concentrated HNO_3 to attack carbonates, then completely digested in a 3:1 mixture of concentrated HF and HNO_3 on a hotplate for 48 hours. Residual fluorides were removed by triplicate treatment with concentrated HNO_3, before final dissolution in 6 mL 7M HCl. Aliquots of these digest solutions were taken for multi-element analysis on a Thermo Element XR at ETH Zürich. Sub-samples were then spiked with a ^{61}Ni–^{62}Ni double spike to achieve a sample-spike ratio of approximately 1 prior to column chromatography. Two different column chromatography procedures were utilised in this study, detailed in Figure 2 and modified following Cameron and Vance (2014), Ciscato et al. (2018) and Archer et al. (2020). For full details, see the Supplementary Information.

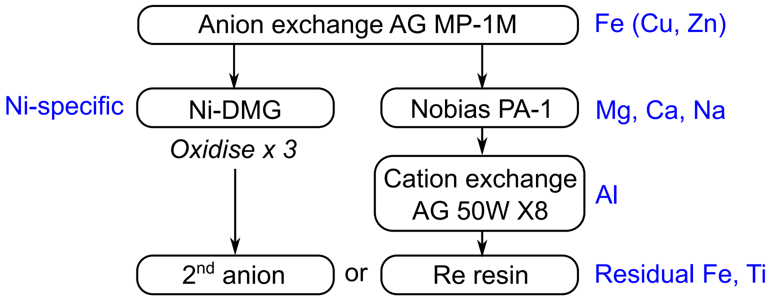

Figure 2. Flowchart illustrating the two alternative Ni column chromatography procedures utilised in this study. Full details given in the Supplementary Information.

Nickel isotope compositions were analysed on a Neptune Plus multi-collector ICP-MS at ETH Zürich (Vance et al., 2016; Ciscato et al., 2018) and are reported relative to the NIST SRM986 Ni standard, as:

$$(2) \qquad \delta^{60/58}\mathrm{Ni} = \left(\frac{(^{60}\mathrm{Ni}/^{58}\mathrm{Ni})_{\mathrm{sample}}}{(^{60}\mathrm{Ni}/^{58}\mathrm{Ni})_{\mathrm{SRM\ 986}}} - 1\right) \times 1000$$

Accuracy and precision of the Ni isotope ratio measurements were monitored by repeated analysis of the primary NIST solution standard at a range of sample:spike ratios (0.2 to 5), and the repeated digestion and analysis of two reference materials, USGS standards Nod P1 (+0.34 ± 0.05‰, 2SD, n = 5) and Nod A1 (+1.06 ± 0.02‰, 2SD, n = 5). The long-term reproducibility (± 0.07‰) was assessed by repeat measurements of primary standards and one of the secondary standards, Nod A1 (digested and passed through the Ni column chemistry), the latter giving δ^{60}Ni = +1.04 ± 0.07‰ (2 SD, n=175 over 4 years), in agreement with previously published results (Gueguen et al., 2016).

4. Results

4.1 Mineralogy and geochemistry

The bulk mineral assemblages of the four MANOP samples analysed by XRD are similar (Table S1, Figs S1-S4). The major mineral phase in all samples is smectite (49 – 60 wt%). Other minerals present in all samples include calcite (0.1 – 22 wt%), plagioclase (13 – 20 wt%), quartz (4 – 6 wt%), halite (4 – 5 wt%), kaolinite (4 – 6 wt%) and barite (1 – 3 wt%). A Mn oxide phase, tentatively identified as birnessite, is present at levels close to the detection limit of the XRD analysis (0.3 – 2 wt%). Muscovite (4 wt%) is identified in the sample from site M (8967, 1–3 cm depth) only, representing the only notable difference between this sample and the deepest sample at site H (5313, 19–21 cm), which are otherwise similar in their phase quantification (Table S1).

Elemental concentrations of the MANOP samples (Table 2, Table S2) are consistent with the mineralogical information. Aluminium and Ti, expected to be present largely in the silicate (i.e. clay mineral) fraction, are somewhat higher at site H (~5 and ~0.3

wt%, respectively) than site M (~4.2 and ~0.2 wt%), reflected in a higher proportion of smectite at site H (Table S1). However, Fe concentrations are elevated at site M (~5.5 wt%) compared to site H (~4 wt%), and Fe/Al ratios at site M are significantly higher than lithogenic values (e.g., upper continental crust, UCC; Fig. 3). Manganese concentrations are high, particularly in the upper 10 cm at site H (at ~5 wt%), dropping to ~2 wt% below this. The deepest sample at site M has a considerably lower Mn content than the other samples, at 0.1 wt%.

Trace metal concentrations (e.g., Ni, Cu, Zn, Mo, Cd), are significantly enriched at both sites H and M relative to expected detrital abundances, e.g., as found in UCC (Table 2, Table S2, Fig. 3), with enrichments typically greater at site H than at site M. There is a coupling between Mn enrichment and those of Ni, Cu and Zn, particularly clear at Site H, where the three shallowest samples (<10 cm depth) are considerably more enriched than the three deeper samples (at 10 – 20 cm) (Fig. 3).

Manganese contents of Nod P1 and the CCZ surface and buried nodules are similar (Table 2), at 31 to 32 wt%, while Fe contents are somewhat lower in buried nodules (at ~3 wt%) than surface nodules (at 4 – 5 wt%). The Peru Basin nodule has an even higher Mn content (at ~48 wt%). Nickel concentrations are highest in the Pacific surface nodules (at ~1.1 wt%) and lower in the deeply buried nodules (at ~0.7–0.8 wt%). As a result, Ni/Mn ratios are lower in buried (~0.025) than surface (~0.038) nodules. For a full discussion of the elemental distribution patterns in the CCZ nodules, see Heller et al. (2018). Atlantic Nod A1, which was collected from a much shallower water depth (776 m; Table 1) than the Pacific nodules, has a lower Mn content (20 wt%), a higher

Fe content (10 wt%) and lower trace element concentrations (e.g., 0.6 wt% Ni, 0.1 wt% Cu), and an intermediate Ni/Mn ratio (0.029).

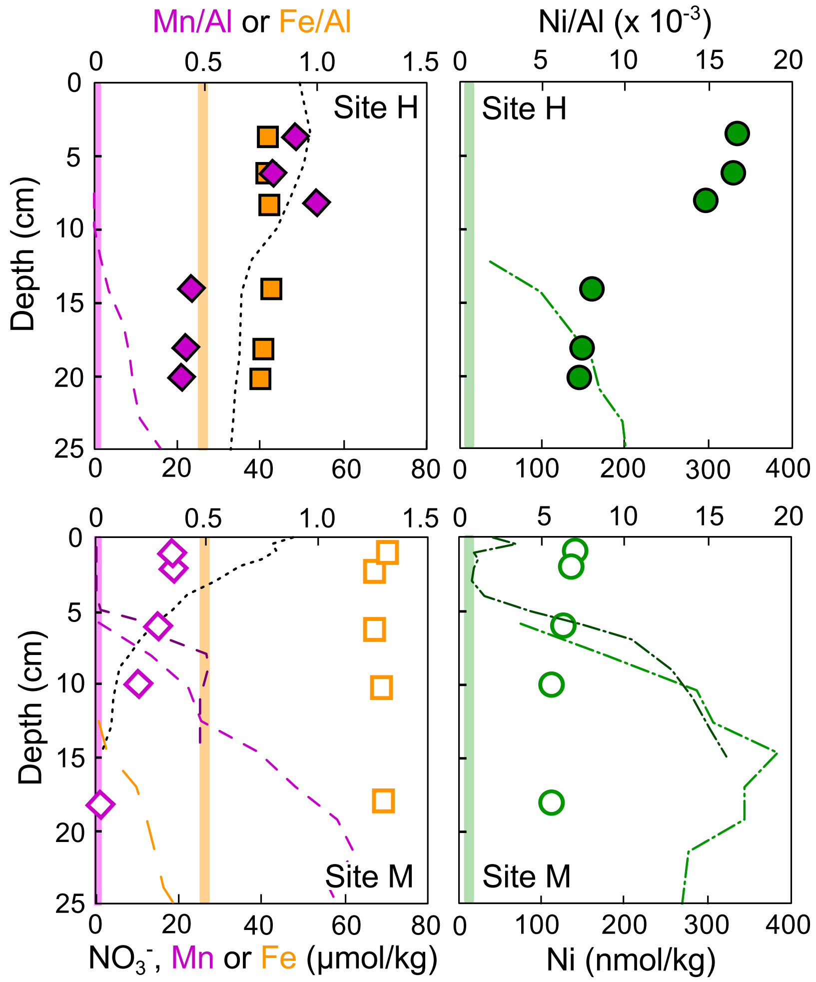

Figure 3. Solid-phase Mn/Al (purple diamonds), Fe/Al (orange squares), and Ni/Al (green circles) ratios in the sediment at the two MANOP sites. Filled symbols – site H, open symbols – site M. Solid coloured bars illustrate upper continental crust Me/Al ratios, from Rudnick and Gao (2003). Porewater concentrations of NO_3^- (black dotted lines), Mn (purple dashed lines), Fe (site M only, orange long dashed line) and Ni (green dot-dashed lines) from Klinkhammer (1980: Site H and M) and Heggie et al. (1986; Site M only: darker coloured lines for Mn, Ni) are overlain on secondary x-axes.

4.2 Ni isotope compositions

The Ni isotope compositions of samples from both MANOP sites are light relative to seawater, ranging from –0.79 to –0.17‰ (Table 2; Fig. 4). δ^{60}Ni values for site H are approximately homogeneous with depth, with mean $\delta^{60}Ni_H$ = –0.21 ± 0.09‰ (2 SD). Site M δ^{60}Ni values are more negative than those of site H, and become isotopically lighter with depth, with $\delta^{60}Ni_M$ from –0.42 to –0.79‰. MANOP δ^{60}Ni values are much more negative than deep seawater, with $\delta^{60}Ni_{seawater}$ = +1.34 ± 0.07‰ (1 SD, seawater samples >200m; Cameron and Vance, 2014; Takano et al., 2017; Wang et al., 2018; Archer et al., 2020), and than Fe-Mn crusts, with $\delta^{60}Ni_{FeMnCrust}$ = +1.62 ± 0.37‰ (1 SD, Gall et al., 2013; Gueguen et al., 2016).

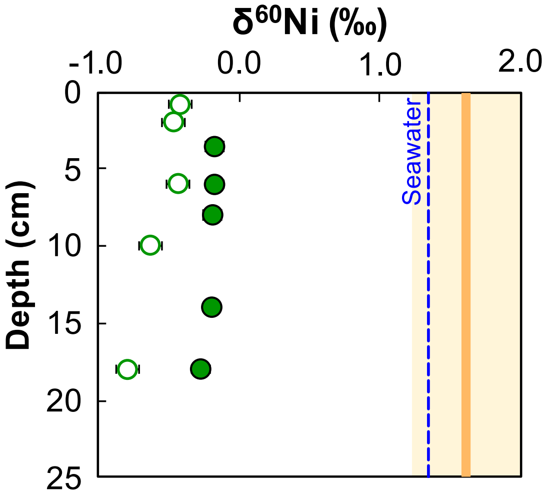

Figure 4. Ni isotope compositions for samples from MANOP site H (filled symbols) and site M (open symbols) with depth in the sediment. Error bars (similar to symbol size) are the long-term reproducibility of the secondary standard (± 0.07‰). Blue dashed line: deep seawater δ^{60}Ni (Cameron and Vance, 2014; Takano et al., 2017; Wang et al., 2018; Archer et al., 2020). Orange solid bar and shaded region: Fe-Mn crust δ^{60}Ni, mean and 1SD (Gall et al., 2013; Gueguen et al., 2016).

The Pacific Mn nodules from the ocean floor (Nod P1, 21KG-1n), which are predominantly phyllomanganates, have δ^{60}Ni values of +0.34 and +0.28‰ (Table 2). The two deeply buried nodules (22KL 530cm and 801cm), comprised mostly of todorokite, have lower δ^{60}Ni values, at –0.08‰ and +0.01‰. The Peru Basin nodule

(77BC11-6) is also predominantly todorokite and is isotopically the lightest of the six nodules, at –0.22‰. Nod A1 from the Atlantic has a heavier Ni isotope composition, at δ^{60}Ni = +1.06‰ (Table 2).

5. Discussion

The sediment samples from the two MANOP sites have the lightest Ni isotope composition yet measured for modern marine sediments (at –0.2 to –0.8‰), considerably lighter than Fe-Mn crusts (about +1.6‰; Gall et al., 2013; Gueguen et al., 2016), organic-rich sediments (about +1.1‰; Ciscato et al., 2018), euxinic sediments from the Black Sea (about +0.2‰; Vance et al., 2016), and the lithogenic Ni isotope composition (about +0.1‰; Cameron et al., 2009). All MANOP samples are also at least 20-fold enriched in Ni compared to the UCC (Fig. 3; Table 2); hence, the lithogenic Ni component in these sediments is minor. We consider two possible origins for isotopically light authigenic Ni: (1) an isotopically light source of Ni or (2) isotope fractionation during diagenesis.

5.1 An isotopically light source of Ni to the MANOP sites?

One possible source of Ni to sediments is from the dissolved pool in seawater; a diffusive flux of Ni was recently suggested to contribute to Ni accumulation in oxygen-deficient continental margin sediments (Ciscato et al., 2018). However, a diffusive flux requires higher Ni concentrations in bottom waters compared to porewaters. Dissolved Ni concentrations measured in core-top porewaters at the MANOP sites are similar to or, at site M, higher than bottom waters (Fig. 3; Klinkhammer, 1980; Heggie et al., 1986), suggesting, if anything, a small benthic flux of Ni *out* of porewaters. Alternatively, Ni in seawater may be scavenged by particulate material in the water column, providing a 'hydrogenetic' source of Ni to sediments. Models of hydrogenetic Fe-Mn crust formation have emphasized the importance of inorganic sorption processes of this type (e.g., Koschinsky and Hein, 2003). If Fe-Mn crusts represent the hydrogenetic Ni source to sediments, Ni that is isotopically similar to or heavier than seawater, at +1.62 ± 0.37‰ (1 SD, Gall et al., 2013; Gueguen et al., 2016) would be expected in the MANOP sediments.

Nickel displays a typical nutrient-type profile in seawater (e.g., Bruland, 1980). Furthermore, a strong correlation with organic carbon is observed in sediments underlying upwelling zones, suggesting organic matter is an important supply route of Ni to sediments (e.g., Fig S7; Ciscato et al., 2018). Cellular Ni/P ratios from the mixed layer of the equatorial Pacific range from 0.25 – 1.15 mmol/mol (measured by synchrotron XRF; Twining et al., 2012), similar to ratios for plankton tows from nearby MANOP sites (0.51 to 0.96 mmol/mol; Collier and Edmond, 1984). Both MANOP sites receive high fluxes of biogenic particulate material, with C_{org} rain rates of 110 – 130 µg $C_{org}/cm^2/yr$ (Lyle et al., 1984). Given these values, we calculate that approximately 5 – 10% of the Ni budget in the MANOP sediments is supplied by organic matter (see Table S3 for details). However, higher particulate Ni/P ratios of about 5 – 15 mmol/mol are observed below the mixed layer in the eastern Pacific (Fig. S5; Ohnemus et al., 2017), suggesting that preferential P remineralisation occurs as organic-rich particles settle through the water column (recently suggested in the context of Cd/P; Bourne et al., 2018). The links between export production and sedimentary metal concentrations is an area of active research, but we note that a particulate Ni/P ratio of ~15 mmol/mol could account for ~100% of the Ni in the MANOP sediments (Table S3).

Organic matter is therefore a significant source of Ni to the MANOP sediments, but is it isotopically light? The limited dataset for upper water column δ^{60}Ni (Takano et al., 2017; Wang et al., 2018; Archer et al., 2020) suggest that phytoplankton do preferentially take up isotopically light Ni. However, the maximum fractionation factor implied by water column data for biological uptake is rather small, at about –0.3‰ (Archer et al., 2020). Consistent with this inference, Takano et al. (2020) estimate the δ^{60}Ni of biogenic particles in the South China Sea to be +0.6 to +1‰. Hence, Ni in organic matter exported from the photic zone is not expected to be nearly light enough to explain the MANOP δ^{60}Ni values (at –0.2 to –0.8‰). Furthermore, modern organic-rich sediments from the Peru margin have bulk Ni isotope compositions of +1.12 ± 0.08‰ (1SD, n = 25; Ciscato et al., 2018), consistent with the water column data and suggesting that particle cycling on transit from the photic zone to sediment is not associated with significant isotopic fractionation. Organic matter cannot explain the light Ni isotope compositions observed at the MANOP sites.

A third possible source of Ni, particularly site M, which is 25 km east of the East Pacific Rise, is hydrothermal sedimentation. To our knowledge, δ^{60}Ni values have not been measured in hydrothermal fluids, but may be expected to be isotopically light, similar to lithogenic Ni, at about +0.1‰ (Cameron et al., 2009). However, a direct Ni source from hydrothermal fluids is unlikely; recent GEOTRACES sections suggest that hydrothermal plumes may instead be sites of Ni removal from seawater via scavenging (discussed by Ciscato et al., 2018). Using an endmember mixing model, Fischer (1983) estimates that ~10% of the Ni (but ~50% of the Fe) at site M (compared to <1% of the Ni at site H) is hydrothermally sourced. We consider a possible role for hydrothermally sourced Fe to sedimentary Ni cycling at site M in section 5.3.

5.2 Nickel isotope fractionation during diagenesis: coupling of Ni-Mn

Having ruled out an isotopically light source of Ni to the sediment, we suggest that post-depositional processes are responsible for the MANOP Ni isotope compositions. First, we consider two processes coupled to Mn diagenesis: (1) cycles of Mn oxide dissolution and reprecipitation (‘Mn cycling’) and (2) transformation of birnessite to todorokite (‘todorokite transformation’).

Manganese cycling

Porewater data from the MANOP sites (Klinkhammer, 1980; Heggie et al., 1986) illustrate the clear coupling between Mn and Ni cycling – via cycles of Mn-oxide dissolution and precipitation (Fig. 3). Sorbed Ni is released to porewaters upon Mn oxide dissolution, and resorbed on newly precipitating Mn oxide phases within the shallower oxygenated zone. Manganese oxides are strong sorbents for divalent trace metals like Ni due to their negative surface layer charge at the pH of natural waters (e.g., Burns and Burns, 1979; Koschinsky and Halbach, 1995). In particular, phyllomanganates like birnessite, which has a layered structure of edge-sharing MnO_6 octahedra, are ubiquitous in the natural environment and are the main Mn-bearing and trace metal-sorbing phases in oxic marine sediments (e.g., Peacock and Sherman, 2007a; Little et al., 2014). Experimental estimates of the magnitude of Ni isotope fractionation on sorption to birnessite suggest a large light isotope effect, with a recent study reporting $\Delta^{60}Ni_{MnO2\text{-}aqueous}$ = –2.8 to –3.4‰ (Sorensen et al., 2020).

The pattern of variation in Ni concentration and isotopic composition across the Black Sea redoxcline (Vance et al., 2016) is qualitatively and quantitatively consistent with these experimental data, with sorption to particulate Mn oxides above the redoxcline preferring the light Ni isotopes by about 4‰. We hypothesize that a similar process takes place in sediment porewaters, explaining (at least in part) the light isotopic compositions of the MANOP sediments. The smaller $\Delta^{60}Ni_{MANOP\text{-}seawater}$ offset of about –1.6 to –2.4‰ compared to experiments and the Black Sea likely reflects the fact that the porewater-sediment system is not completely open.

In the context of the experimental data, the observations in the Black Sea, and the new data here, the published data for hydrogenetic Fe-Mn crusts stand out as different. Most Fe-Mn crusts analysed to date are isotopically similar to or heavier than seawater (Fig. 5A). Sorensen et al. (2020) suggest three possible explanations for this observation. The first involves differences in the mechanism of incorporation into the solid structure. Nickel in slow-growing Fe-Mn crusts is predominantly structurally incorporated into birnessite (specifically vernadite/δ-MnO_2) vacancy sites (Peacock and Sherman, 2007a), while adsorption in experiments occurs primarily as a triple-corner-sharing surface complex over the vacancy sites (Peacock and Sherman, 2007b; Sorensen et al., 2020). Surface complexation is also likely to be dominant in dynamic open system environments like the redoxcline of the Black Sea. It is possible, therefore, that structural incorporation of Ni is associated with a different isotope effect than adsorption as a surface complex. A second explanation relates to reaction kinetics, with slow-growing (a few mm/Ma) Fe-Mn crusts exhibiting long-term isotopic equilibration of Ni with seawater; exchangeability of Ni in Fe-Mn crusts has recently been demonstrated by Hens et al. (2019). Finally, it has been suggested that Ni speciation in seawater may control the isotopic composition of the sorbing Ni species, with a possible role for organic complexation (Sorensen et al., 2020).

Fe-Mn crusts are not only marked by relatively positive δ^{60}Ni values, but also by significant variability in δ^{60}Ni (Fig. 5A, +0.41 to +2.47‰; Gall et al., 2013), which may reflect the complexities of the aforementioned processes. We note, however, that a depth profile through one crust (ZEP2-DR05-04) from the Pacific Ocean shows a marked transition towards much lighter Ni isotope compositions coupled to decreasing Mn/Ni ratios at depth (Fig. 5B; Gueguen et al., 2016). The authors attributed this transition to lighter isotopic compositions to the reductive dissolution of primary Mn oxide phases followed by their reprecipitation and the resorption of Ni in an open system (Gueguen et al., 2016) – i.e. the same process of Mn cycling described here.

Phyllomanganate-rich surface Mn nodules may also record the impact of Mn cycling in their Ni isotope compositions, because they contain Ni from both hydrogenetic and diagenetic sources. They consist of hydrogenetic layers formed by precipitation from seawater (vernadite/δ-MnO_2 and amorphous FeOOH) and diagenetic layers formed during re-precipitation from sub-oxic porewaters (primarily 7 and 10 Å birnessite) (e.g., Koschinsky and Halbach, 1995; Heller et al., 2018). These nodules are variably isotopically light (at +0.28 to +1.06‰) compared to seawater, and fall close to the Mn/Ni v δ^{60}Ni evolution line of the Fe-Mn crust affected by Mn cycling (Fig. 5B, Gueguen et al., 2016).

Overall, a consistent picture of the impact of Mn cycling on Ni isotope compositions emerges from the MANOP sediments, Fe-Mn crusts and Mn nodules. Hydrogenetic δ^{60}Ni values (represented by Fe-Mn crusts) are similar to the seawater Ni isotope composition, with Mn cycling during diagenesis leading to partial dissolution and reprecipitation of phyllomanganates that re-scavenge isotopically light Ni in a variably open system, associated with decreasing Mn/Ni ratios.

Todorokite transformation

During diagenesis, birnessite can also transform (via a 10 Å phase) to the tectomanganate todorokite (Atkins et al., 2014; Wegorzewski et al., 2020). Recent experimental work suggests that this transformation leads to significant Ni release to porewaters, because Ni is not significantly incorporated in the todorokite crystal structure (Atkins et al., 2016). Consistent with this finding, buried Mn nodules of todorokite exhibit *higher* Mn/Ni ratios compared to phyllomanganate-rich surface nodules (Fig. 5B; Heller et al., 2018; Wegorzewski et al., 2020), i.e. the opposite evolution to that inferred for Mn cycling. Furthermore, buried nodules are isotopically even lighter (at –0.22 to +0.01‰) than surface nodules (at +0.28 to +1.06‰), suggesting that todorokite transformation may lead to further Ni isotope fractionation.

However, the relevance of todorokite transformation to the Ni isotope composition of the MANOP sediments, and to marine Ni cycling more broadly, remains unclear, because the timescale and mechanism of todorokite transformation and its prevalence in marine sediments is difficult to establish. Typically considered a process of phyllomanganate ageing under oxic conditions, oxic transformation of birnessite to todorokite in the lab has only been achieved at higher than ambient temperatures and/or lower than circumneutral pH (e.g., Atkins et al., 2014). Recently, Jung et al. (2020) demonstrate that cyclic redox fluctuations (driven in the lab by cyclic voltammetry) can also trigger the layer-to-tunnel phase transformation. Cyclic redox fluctuations are common in marine sediments, suggesting that todorokite transformation may occur outside of fully oxic diagenetic settings. Nevertheless, identification of todorokite by XRD is currently impossible at the low abundances present in marine sediments, due to the similar crystallographic structure of different Mn oxide polymorphs. While our XRD data for the MANOP sediments indicates the presence of a phyllomanganate phase, we cannot rule out the occurrence of more crystalline todorokite at low abundance. Geochemically, MANOP Mn/Ni ratios are more similar to those of the buried, todorokite-rich Mn nodules than to surface nodules, but they are also similar to hydrogenetic Pacific Fe-Mn crusts (Fig. 5B).

Future experimental work will test the hypothesis that todorokite transformation leads to preferential retention of isotopically light Ni in the solid phase, and investigate the relationships between the transformation mechanism, Ni release, and evolving Mn/Ni ratios.

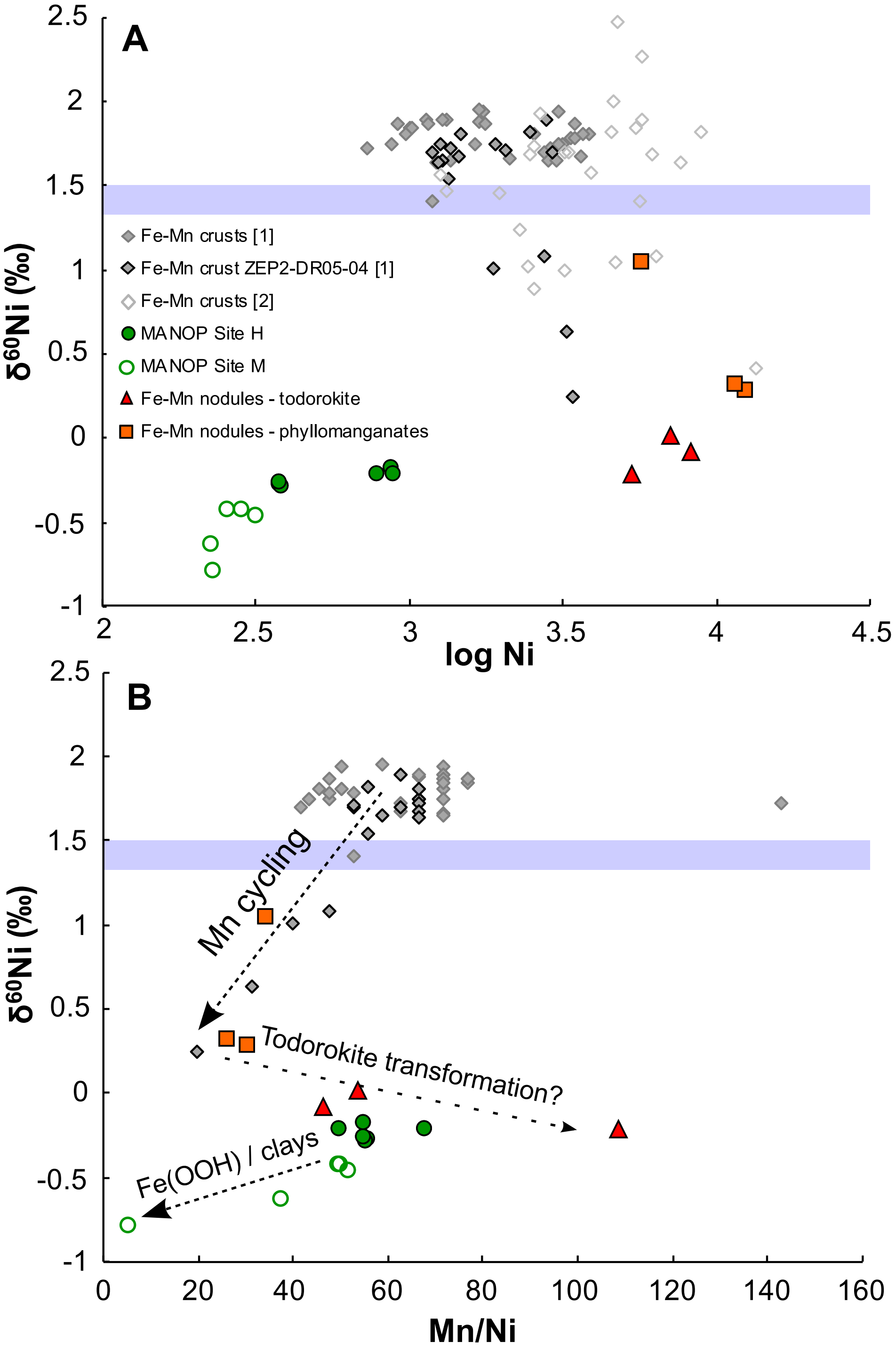

Figure 5. A) log Ni concentration and B) Mn/Ni ratios versus δ^{60}Ni values for samples from MANOP site H (green filled circles), MANOP site M (green open circles), Mn nodules of predominantly phyllomanganates (orange squares) and todorokite (red triangles), and literature values for Fe-Mn crusts (grey diamonds). Labelled dashed arrows in B represent the proposed diagenetic effects of Mn cycling, todorokite transformation, and scavenging by Fe (hydr)oxides or authigenic clays (see text for details). Error bars on δ^{60}Ni values are approximately the size of the symbols (± 0.07‰). Literature data: [1] Gueguen et al. (2016) and [2] Gall et al. (2013) (Note: No Mn data are presented by Gall et al., 2013).

5.3 Nickel isotope fractionation during diagenesis: Fe (hydr)oxides or authigenic clays?

We suggest that the diagenetic cycling of Ni coupled to Mn is the key control on the Ni isotope compositions of the MANOP sediments. However, the sample with the lightest Ni isotope composition (at –0.79‰), from 18 cm depth at site M, has the lowest Mn concentration (0.12 wt%) and lowest Mn/Ni ratio (5.4, Fig. 5B). Despite limited Mn enrichment, this sample is significantly Ni enriched ($Ni/Al = 0.0056$ cf. $Ni/Al_{UCC} = 0.0006$). Together, these observations suggest an additional control on Ni isotope compositions in low Mn sediments. We consider two possibilities: (1) sorption of isotopically light Ni on nanoscale Fe (hydr)oxides, and (2) incorporation of isotopically light Ni in Fe-rich authigenic clays.

Nanoscale Fe oxides

Iron is significantly more enriched at site M (Fe/Al ~ 1.3) compared to site H (Fe/Al ~0.8; Fig. 3), with the difference attributed to the presence of hydrothermal precipitates at site M (Fischer, 1983). Sorption of Ni on Fe (hydr)oxides is less energetically favoured than on phyllomanganates, due to the higher pH_{pzc} for Fe (hydr)oxide phases (at about 7 to 8) compared to MnO_2 (at about 2, Stumm and Morgan, 1996; Tripathy and Kanungo, 2005). Nevertheless, when phyllomanganates are scarce, Fe (hydr)oxide phases become environmentally relevant.

Experimental investigations of Ni isotope fractionation on sorption to ferrihydrite found $\Delta^{60}Ni_{ferrihydrite\text{-}aqueous} = –0.35‰$ (Wasylenki et al., 2015; Gueguen et al., 2018). For Ni coprecipitation with ferrihydrite, Wang and Wasylenki (2017) found that the fractionation factor increased from –0.08 to –0.50‰ with increased co-precipitation (e.g., at higher pH). Sorption to goethite is associated with a larger fractionation factor, $\Delta^{60}\mathrm{Ni}_{\mathrm{goethite\text{-}aqueous}} = -0.77$‰ (Gueguen et al., 2018). A correlation is observed between Fe/Ni and Ni isotope compositions at site M (Fig. 6A), consistent with the hypothesis of scavenging of isotopically light Ni by Fe (hydr)oxide phases. We envisage that this process occurs during diagenesis, due to the evolution towards lighter Ni isotope compositions at site M compared to site H. (Fig. 6A) However, it is also feasible that dissolved Ni is scavenged by hydrothermal Fe precipitates suspended in the water column and which subsequently settle out.

Interestingly, δ^{60}Ni also correlates with published δ^{98}Mo values for the MANOP samples (Fig 6B; Poulson Brucker et al., 2009). Like Ni, Mo cycling has been strongly linked to Mn in oxic marine sediments, but a role for sorption to Fe (hydr)oxides in the oceanic Mo cycle has also been proposed (Goldberg et al., 2009). Molybdenum sorption on Mn oxides exhibits a stronger preference for light isotopes (e.g., Barling and Anbar, 2004) than Mo sorption on Fe (hydr)oxides (Goldberg et al., 2009). Thus, these two competing controls on Mo isotope compositions appear to be consistent with the MANOP δ^{98}Mo values, in which the site M samples (rich in Fe) are isotopically heavier than those of site H (rich in Mn).

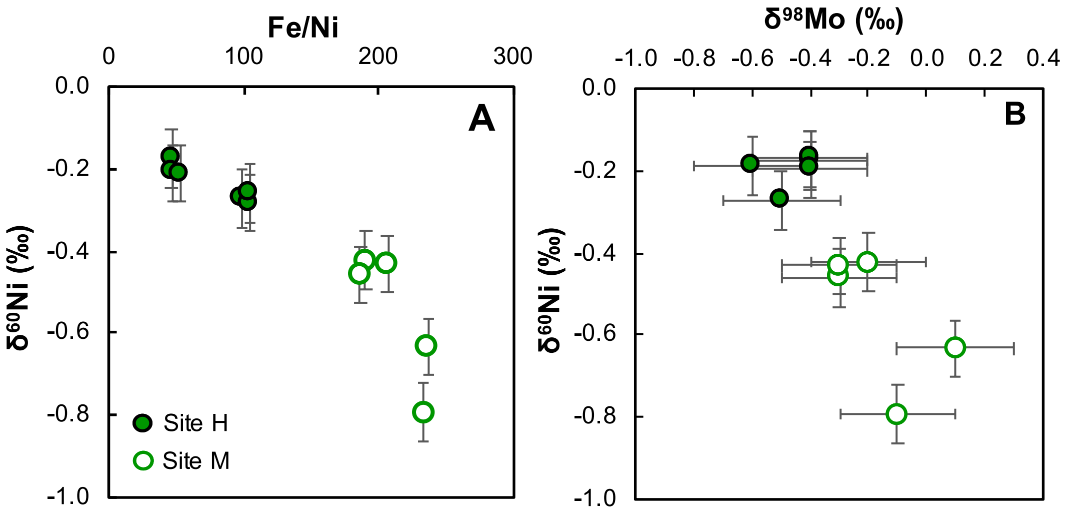

Figure 6. Relationships between A. Fe/Ni and B. δ^{98}Mo (data: Poulson Brucker et al., 2009) and Ni isotope compositions at the two MANOP sites. Error bars on δ^{60}Ni are the long-term reproducibility (± 0.07‰) and on δ^{98}Mo are ± 0.20‰ (the estimated external reproducibility on bulk δ^{98}Mo values from Poulson Brucker et al., 2009).

Authigenic clay minerals

Though it has long been inferred that authigenic Fe (hydr)oxide coatings are an important host phase for trace elements in marine sediments, direct image-based identification of these phases has proven challenging. The XRD technique utilised in this study, for example, has a detection limit of ~2 wt% for Fe (hydr)oxide phases. However, it has been suggested that part of the challenge in directly observing Fe (hydr)oxide coatings reflects the fact that authigenic Fe is (at least partly) hosted in authigenic clay minerals (e.g., Abbott et al., 2019). By extension, it is possible that Fe (hydr)oxides are not as quantitatively important scavengers of trace elements, and that authigenic clay minerals play an under-appreciated role (e.g., Hein et al., 1979; Abbott et al., 2019).

The dominant mineral phase at both MANOP sites is smectite; indeed, authigenic smectite (Fe-rich montmorillonite) makes up 26 to 66% of the clays present in north equatorial Pacific sediments (Hein et al., 1979). Hein et al. (1979) found that this smectite contains 70 – 150 µg/g Ni, though the clay fraction analysed may have included sorbed nanoscale Fe (hydr)oxides. Nevertheless, using x-ray absorption spectroscopy, Merrot et al. (2019) find that Ni is primarily hosted by Fe-rich smectite and early diagenetic greenalite in lagoon sediments. During terrestrial weathering, Ni liberated from primary minerals is concentrated by smectite, where present (e.g., Ratié et al., 2018). Furthermore, the smectitic zone of a weathering profile is characterized by light Ni isotope compositions compared to the protolith (Ratié et al., 2018), consistent with experimental results indicating a small light isotope effect on sorption to Na-montmorillonite (a form of smectite), of –0.11 ± 0.09‰ (Spivak-Birndorf et al., 2018). We suggest that better evaluation of the role of authigenic clays in sedimentary trace element budgets should be a target for future research.

5.4 Implications for whole oceanic mass balance

Assuming steady state, there is a significant flux and isotopic mass imbalance in the oceanic Ni cycle, summarised most recently by Ciscato et al. (2018). In their analysis, the input of Ni (riverine dissolved Ni and Ni from mineral dust) is 3.7×10^8 mol/year, with $\delta^{60}Ni_{input} = +0.79‰$. By contrast, the estimated output flux to sediments ranges from 7.2 to 17×10^8 mol/year (i.e. 2–5 times larger than the estimated input flux), with $\delta^{60}Ni_{output} \approx +1.5‰$. By far the dominant feature of the existing Ni budget is the removal flux to dispersed Fe-Mn oxides in ‘oxic sediments’ (where oxygen penetrates to >1 cm depth; Morford and Emerson, 1999), which is estimated to range from 5.8 to 10.5×10^8 mol/yr (Gall et al., 2013; Cameron and Vance, 2014). The isotopic composition of this oxic sink has been assumed to reflect that of Fe-Mn crusts, at about +1.6‰.

Ciscato et al. (2018) suggest that the previously assumed flux of Ni to the oxic sink, and its isotopic composition, might be erroneous. Balancing the budget would require an oxic sink of 1.8 x 10^8 mol/yr (3–5 times smaller than previously estimated), with an average isotopic composition of about +0.5‰. Our study suggests a resolution of this problem, via the diagenetic remobilization of isotopically heavy Ni and its release into bottom waters. From here on, we assume that this diagenetic remobilization and release occurs in sub-oxic (specifically, Mn reducing) settings. However, we note that todorokite transformation may also occur in oxic settings, and thus this process may be significantly underrepresented in the following assessment.

First, we recalculate the Ni burial flux in oxic sediments by coupling to estimates for Mn. The authigenic accumulation rate of Mn in pelagic clays is estimated at 6 – 23 μmol/cm^2/kyr (best guess: 13 μmol/cm^2/kyr) (Rehkämper and Nielsen, 2004 and references therein). The Ni/Mn ratio of the MANOP site H sediments and of Fe-Mn crusts is 0.019 (by weight; USGS compilation of Manheim and Lane-Bostwick, 1991). Of the sediment types described in the marine sediment census of Dutkiewicz et al. (2015), we include only 'clay' (40.2% ocean area) in this category. The remainder are predominantly calcareous oozes, which have a low Mn content (Morford and Emerson, 1999 and references therein), though we note that two 'transitional' sediment types ('siliceous mud', 5.0% and 'fine-grained calcareous sediment', 12.4%; Dutkiewicz et al., 2015) may be a significant Mn sink and should be a target of future studies. We estimate a Ni burial flux to oxic sediments (in this case, exclusively clay) of 1.5 to 5.9 x 10^8 mol/yr (Table 3). Nickel burial in association with carbonates is negligible on this scale, at about 0.14 x 10^8 mol/year (Ciscato et al., 2018). Following previous authors, we assume that the Ni isotope composition of oxic sediments is represented by Fe-Mn crusts, at +1.62 ± 0.37‰ (1 SD, Table 3; Gall et al., 2013; Gueguen et al., 2016).

Next, we estimate the benthic return flux of Ni *from* sub-oxic sediments, also by comparison to Mn. Morford and Emerson (1999) estimate that sub-oxic sediments (defined as those deposited at >1000 m water depth for which oxygen penetrates to ≤1 cm) cover ~4% of the ocean area. They estimate a sub-oxic benthic Mn flux of 0.7 –1.3 x 10^{10} mol/yr (Morford and Emerson, 1999). Our study suggests that Mn diagenesis leads to preferential retention of Ni in sediments compared to Mn (Fig. 5B), but todorokite transformation should have the opposite effect (Fig. 5B; Atkins et al., 2016). Direct measurements of porewater Ni/Mn ratios for the MANOP sediments are variable, but generally similar to the solid phase (i.e. ~0.019) ranging from 0.005 – 0.031 (mean site M = 0.009, mean site H = 0.020; Klinkhammer, 1980). For an estimated Ni/Mn range of 0.009 – 0.020, we calculate a benthic Ni flux of 0.6 – 2.3 x 10^8 mol/yr.

Next, we solve for the isotopic composition of the benthic flux by expanding equation (1) for all known fluxes and assuming steady state, where:

$$(3) \qquad F_{river}\delta_{river} + F_{dust}\delta_{dust} + F_{benthic}\delta_{benthic} = F_{oxic}\delta_{oxic} + F_{org}\delta_{org} + F_{eux}\delta_{eux} + F_{carb}\delta_{carb}$$

In equation (3), the Ni sources include rivers, dust and the benthic flux, while the sinks are pelagic clays (‘oxic’), organic-rich sediments on continental margins (‘org’), euxinic sediments (‘eux’) and carbonates (‘carb’).

We carry out a Monte Carlo simulation (10,000 iterations), allowing each flux to vary within its given range (flux and δ^{60}Ni; values given in italics in Table 3) and solving for the benthic flux required to balance the Ni mass budget (model results in bold in Table 3). Flux magnitudes were forced by uniformly distributed random numbers, and isotopic compositions by normally distributed random numbers (around the mean and standard deviation of published data, see Table 3). For further discussion of the approach, see the Supplementary Information. Note that the carbonate and euxinic sinks, and the dust source, are minor, and therefore represented in the simulation simply by the best guess at their magnitudes and isotopic compositions (Table 3). The riverine flux is included as the concentration and discharge-weighted average of Cameron and Vance (2014). Post-simulation, the benthic flux range was restricted to 0.6 – 2.3 x 10^8 mol/yr, with the side effect of reducing the maximum output flux to pelagic clays to 4.6 x 10^8 mol/yr (see SI for further discussion).

This analysis suggests that the isotopic composition of the benthic flux required to balance the oceanic Ni budget is approximately +3‰ (Table 3). Compared to the isotopic composition of oxic sediments (at +1.6‰), this equates to an effective fractionation factor for diagenesis of about –1.4‰ (averaged globally). This value is comparable to the observed isotopic difference between the MANOP sediments (at about –0.2 to –0.8‰) and the possible sources of Ni to the site (at about +0.1 to +1.6‰; Section 5.1), supporting the hypothesis that diagenetic remobilisation of isotopically heavy Ni can balance the oceanic Ni budget.

Table 3. Modelled oceanic mass balance of Ni and Ni isotopes (see text and SI for full details). Values in italics were used in the Monte Carlo simulation. Values in bold are outputs from the model.

	Flux (×10^8 mol/yr)		δ^{60}Ni (‰)	
	Range	Best guess	Mean and SD or range	Best guess
Source fluxes				
Rivers[a]	-	*3.60*	-	*0.8*
Dust[b,c]	-	*0.076*	–0.09 to 0.37	*0.14*
Benthic	*0.6 to 2.3*	**1.44**	**3.17 ± 1.08**	**3.03**[*]
Sink fluxes				
Pelagic clays	*1.5 to* ***4.6*** *(5.9)*	**3.08**	*1.62 ± 0.37*[d]	*1.62*
Organic-rich[b]	*1.1 to 2.4*	**1.74**	*1.12 ± 0.08*	*1.12*
Carbonates[b]	0.031 to 0.44	*0.14*	1.10 to 1.64	*1.29*
Euxinic[b]	0.093 to 0.25	*0.15*	0.3 to 0.6[c]	*0.45*
Total in/out	**4.3 to 6.0**	**5.1**	**1.41 ± 0.23**	**1.40**
Residence time[1]	**18 to 25 kyr**	**21 kyr**		

[*] Best guess δ^{60}Ni is the median value output by the model (For details see SI, Fig. S8).

[1] Residence time calculated given a global ocean volume of 1.35 × 10^{21} kg and mean Ni concentration of 8 nM (i.e. 1.08 × 10^{13} moles Ni).

References: [a]Cameron and Vance (2014), [b]Ciscato et al. (2018), [c]Vance et al. (2016), [d]Gall et al. (2013).

6. Conclusions

We report Ni isotope compositions for metalliferous sediments from two of the eastern Pacific MANOP sites. Both sites exhibit very light Ni isotope compositions (at –0.8 to –0.2‰) compared to hydrogenetic Fe-Mn crusts (at +1.6‰). Low but variable δ^{60}Ni values are also observed for Mn nodules (–0.2 to +1.0‰). We propose two primary mechanisms to explain the isotopically light diagenetic Ni 'fingerprint': (1) Mn cycling, in which Ni cycling is coupled to the redox-driven dissolution and reprecipitation of Mn oxides, and (2) the mineralogical transformation of birnessite to todorokite, which may occur in oxic or sub-oxic sedimentary environments. In Mn-poor oxic sediments we suggest that additional Ni (and Mo) isotope fractionation accompanies the scavenging of isotopically light Ni by nanoscale Fe (hydr)oxides or Fe-rich authigenic clays.

We hypothesize that diagenetic remobilization of isotopically heavy Ni balances the oceanic Ni budget. Based on estimates for Mn, we calculate a benthic Ni flux of 0.6 to 2.3 × 10^8 mol/yr, comparable in magnitude to the riverine Ni flux, at 3.6 × 10^8 mol/yr. The required isotopic composition of this benthic flux to balance the oceanic Ni budget is approximately +3‰, providing a testable hypothesis for future studies. Our calculation does not directly consider the under-constrained possibility of Ni release during the transformation of phyllomanganates to todorokite in oxic marine sediments, a process that would not be associated with a benthic Mn flux. Further lab and field-based investigations are underway targeting the analysis of oxic and sub-oxic sediments and porewaters, and to investigate the Ni isotope fractionation associated with todorokite transformation.

Acknowledgements

We would like to thank Francis Albarède and an anonymous reviewer for their comments on a previous version of this paper. SHL is supported by a NERC independent research fellowship (NE/P018181/1). ETH involvement in this research was supported by the Swiss National Science Foundation (SNF) through grants 200020-16590 and 200021_184873/1 (to DV). JM’s contributions were supported by NSF grant 1657832. The authors would like to thank Emily Ciscato and Aditi Chatterjee for helpful discussions during the project, Rhian O’Callaghan for making Figure 1, Caroline Peacock for feedback on an earlier version of the manuscript, and Matthias Haeckel for providing the Peru Basin nodule sample (77BC11-6).

References

Abbott, A.N., Löhr, S., Trethewy, M., 2019. Are Clay Minerals the Primary Control on the Oceanic Rare Earth Element Budget? Front. Mar. Sci. 6, 1–19. https://doi.org/10.3389/fmars.2019.00504

Archer, C., Vance, D., Lohan, M.C., Milne, A., 2020. The oceanic biogeochemistry of nickel and its isotopes: new data from the South Atlantic and the Southern Ocean biogeochemical divide. Earth Planet. Sci. Lett.

Atkins, A.L., Shaw, S., Peacock, C.L., 2016. Release of Ni from birnessite during transformation of birnessite to todorokite: Implications for Ni cycling in marine sediments. Geochim. Cosmochim. Acta 189, 158–183. https://doi.org/10.1016/j.gca.2016.06.007

Atkins, A.L., Shaw, S., Peacock, C.L., 2014. Nucleation and growth of todorokite from birnessite: Implications for trace-metal cycling in marine sediments. Geochim. Cosmochim. Acta 144, 109–125. https://doi.org/10.1016/j.gca.2014.08.014

Barling, J., Anbar, A.D., 2004. Molybdenum isotope fractionation during adsorption by manganese oxides. Earth Planet. Sci. Lett. 217, 315–329. https://doi.org/10.1016/S0012-821X(03)00608-3

Bourne, H.L., Bishop, J.K.B., Lam, P.J., Ohnemus, D.C., 2018. Global Spatial and Temporal Variation of Cd:P in Euphotic Zone Particulates. Global Biogeochem. Cycles. https://doi.org/10.1029/2017GB005842

Bruland, K.W., 1980. Oceanographic distributions of cadmium, zinc, nickel and copper in the North Pacific. Earth Planet. Sci. Lett. 47, 176–198.

Burns, R.G., Burns, V.M., 1979. Manganese oxides, in: Burns, R.G. (Ed.), Marine Minerals. pp. 1–46.

Cameron, V., Vance, D., 2014. Heavy nickel isotope compositions in rivers and the oceans. Geochim. Cosmochim. Acta 128, 195–211. https://doi.org/10.1016/j.gca.2013.12.007

Cameron, V., Vance, D., Archer, C., House, C.H., 2009. A biomarker based on the stable isotopes of nickel. Proc. Natl. Acad. Sci. 106, 10944–10948. https://doi.org/10.1073/pnas.0900726106

Ciscato, E.R., Bontognali, T.R.R., Vance, D., 2018. Nickel and its isotopes in organic-rich sediments: implications for oceanic budgets and a potential record of ancient seawater. Earth Planet. Sci. Lett. 494, 239–250. https://doi.org/10.1016/j.epsl.2018.04.061

Collier, R., Edmond, J., 1984. The trace element geochemistry of marine biogenic particulate matter. Prog. Oceanogr. 13, 113–199. https://doi.org/10.1016/0079-6611(84)90008-9

Dutkiewicz, A., Müller, R.D., O'Callaghan, S., Jónasson, H., 2015. Census of seafloor sediments in the world's ocean. Geology 43, 795–798. https://doi.org/10.1130/G36883.1

Fischer, K., 1983. Particle Fluxes in the Eastern Tropical Pacific Ocean - Sources and Processes. Oregon State University.

Gall, L., Williams, H.M., Siebert, C., Halliday, A.N., Herrington, R.J., Hein, J.R., 2013. Nickel isotopic compositions of ferromanganese crusts and the constancy of deep ocean inputs and continental weathering effects over the Cenozoic. Earth Planet. Sci. Lett. 375, 148–155. https://doi.org/10.1016/j.epsl.2013.05.019

Goldberg, T., Archer, C., Vance, D., Poulton, S.W., 2009. Mo isotope fractionation during adsorption to Fe (oxyhydr)oxides. Geochim. Cosmochim. Acta 73, 6502–6516. https://doi.org/10.1016/j.gca.2009.08.004

Gueguen, B., Rouxel, O., Rouget, M.L., Bollinger, C., Ponzevera, E., Germain, Y., Fouquet, Y., 2016. Comparative geochemistry of four ferromanganese crusts from the Pacific Ocean and significance for the use of Ni isotopes as paleoceanographic tracers. Geochim. Cosmochim. Acta 189, 214–235. https://doi.org/10.1016/j.gca.2016.06.005

Gueguen, B., Sorensen, J. V., Lalonde, S. V., Peña, J., Toner, B.M., Rouxel, O., 2018. Variable Ni isotope fractionation between Fe-oxyhydroxides and implications for the use of Ni isotopes as geochemical tracers. Chem. Geol. https://doi.org/10.1016/j.chemgeo.2018.01.023

Heggie, D., Kahn, D., Fischer, K., 1986. Trace metals in metalliferous sediments, MANOP Site M: interfacial pore water profiles. Earth Planet. Sci. Lett. 80, 106–116. https://doi.org/10.1016/0012-821X(86)90023-3

Hein, J.R., Yeh, H.-W., Alexander, E., 1979. Origin of Iron-Rich Montmorillonite from the Manganese Nodule Belt of the North Equatorial Pacific. Clays Clay Miner. 27, 185–194. https://doi.org/10.1346/ccmn.1979.0270303

Heller, C., Kuhn, T., Versteegh, G.J.M., Wegorzewski, A. V., Kasten, S., 2018. The geochemical behavior of metals during early diagenetic alteration of buried manganese nodules. Deep. Res. Part I Oceanogr. Res. Pap. 142, 16–33. https://doi.org/10.1016/j.dsr.2018.09.008

Hens, T., Brugger, J., Etschmann, B., Paterson, D., Brand, H.E.A., Whitworth, A., Frierdich, A.J., 2019. Nickel exchange between aqueous Ni(II) and deep-sea ferromanganese nodules and crusts. Chem. Geol. 528, 119276. https://doi.org/10.1016/J.CHEMGEO.2019.119276

Jaun, B., Thauer, R.K., 2007. Methyl-Coenzyme M Reductase and its Nickel Corphin Coenzyme F430in Methanogenic Archaea, in: Nickel and Its Surprising Impact in Nature. https://doi.org/10.1002/9780470028131.ch8

Jung, H., Taillefert, M., Sun, J., Wang, Q., Borkiewicz, O.J., Liu, P., Yang, L., Chen, S., Chen, H., Tang, Y., 2020. Redox Cycling Driven Transformation of Layered Manganese Oxides to Tunnel Structures. J. Am. Chem. Soc. https://doi.org/10.1021/jacs.9b12266

Kadko, D.C., 1981. A detailed study of uranium-series nuctides for several sediment reaimes of the Pacific. Columbia University.

Kessler, W.S., 2006. The circulation of the eastern tropical Pacific: A review. Prog. Oceanogr. https://doi.org/10.1016/j.pocean.2006.03.009

Klinkhammer, G.P., 1980. Early diagenesis in sediments from the eastern equatorial Pacific, II. Pore water metal results. Earth Planet. Sci. Lett. 49, 81–101. https://doi.org/10.1016/0012-821X(80)90151-X

Koschinsky, A., Halbach, P., 1995. Sequential leaching of marine ferromanganese precipitates: Genetic implications. Geochim. Cosmochim. Acta 59, 5113–5132. https://doi.org/10.1016/0016-7037(95)00358-4

Koschinsky, A., Hein, J.R., 2003. Uptake of elements from seawater by ferromanganese crusts: Solid-phase associations and seawater speciation. Mar. Geol. 198, 331–351. https://doi.org/10.1016/S0025-3227(03)00122-1

Krishnaswami, S., 1976. Authigenic transition elements in Pacific pelagic clays. Geochim. Cosmochim. Acta 40, 425–434. https://doi.org/10.1016/0016-7037(76)90007-7

Little, S.H., Sherman, D.M., Vance, D., Hein, J.R., 2014. Molecular controls on Cu and Zn isotopic fractionation in Fe-Mn crusts. Earth Planet. Sci. Lett. 396, 213–222. https://doi.org/10.1016/j.epsl.2014.04.021

Lyle, M., Heath, G.R., Robbins, J.M., 1984. Transport and release of transition elements during early diagenesis: Sequential leaching of sediments from

MANOP Sites M and H. Part I. pH 5 acetic acid leach. Geochim. Cosmochim. Acta 48, 1705–1715. https://doi.org/10.1016/0016-7037(84)90026-7

Manheim, F.T., Lane-Bostwick, C., 1991. Chemical composition of ferromanganese crusts in the world ocean: a review and comprehensive chemical composition of ferromanganese crusts in the world ocean: a review and comprehensive database. Woods Hole, MA.

Merrot, P., Juillot, F., Noël, V., Lefebvre, P., Brest, J., Menguy, N., Guigner, J.M., Blondeau, M., Viollier, E., Fernandez, J.M., Moreton, B., Bargar, J.R., Morin, G., 2019. Nickel and iron partitioning between clay minerals, Fe-oxides and Fe-sulfides in lagoon sediments from New Caledonia. Sci. Total Environ. 689, 1212–1227. https://doi.org/10.1016/j.scitotenv.2019.06.274

Morford, J.L., Emerson, S., 1999. The geochemistry of redox sensitive trace metals in sediments. Geochim. Cosmochim. Acta 63, 1735–1750. https://doi.org/10.1016/S0016-7037(99)00126-X

Ohnemus, D.C., Rauschenberg, S., Cutter, G.A., Fitzsimmons, J.N., Sherrell, R.M., Twining, B.S., 2017. Elevated trace metal content of prokaryotic communities associated with marine oxygen deficient zones. Limnol. Oceanogr. 62, 3–25. https://doi.org/10.1002/lno.10363

Palenik, B., Brahamsha, B., Larimer, F.W., Land, M., Hauser, L., Chain, P., Lamerdin, J., Regala, W., Allen, E.E., McCarren, J., Paulsen, I., Dufresne, A., Partensky, F., Webb, E.A., Waterbury, J., 2003. The genome of a motile marine Synechococcus. Nature. https://doi.org/10.1038/nature01943

Peacock, C.L., Sherman, D.M., 2007a. Crystal-chemistry of Ni in marine ferromanganese crusts nodules. Am. Mineral. 92, 1087–1092. https://doi.org/10.2138/am.2007.2378

Peacock, C.L., Sherman, D.M., 2007b. Sorption of Ni by birnessite: Equilibrium controls on Ni in seawater. Chem. Geol. 238, 94–106. https://doi.org/10.1016/j.chemgeo.2006.10.019

Poulson Brucker, R.L., McManus, J., Severmann, S., Berelson, W.M., 2009. Molybdenum behavior during early diagenesis: Insights from Mo isotopes. Geochemistry, Geophys. Geosystems 10. https://doi.org/10.1029/2008GC002180

Price, N.M., Morel, F.M.M., 1991. Colimitation of phytoplankton growth by nickel and nitrogen. Limnol. Oceanogr. https://doi.org/10.4319/lo.1991.36.6.1071

Ragsdale, S.W., 2009. Nickel-based enzyme systems. J. Biol. Chem. 284, 18571–

18575. https://doi.org/10.1074/jbc.R900020200

Ratié, G., Garnier, J., Calmels, D., Vantelon, D., Guimarães, E., Monvoisin, G., Nouet, J., Ponzevera, E., Quantin, C., 2018. Nickel distribution and isotopic fractionation in a Brazilian lateritic regolith: Coupling Ni isotopes and Ni K-edge XANES. Geochim. Cosmochim. Acta 230, 137–154. https://doi.org/10.1016/j.gca.2018.03.026

Rehkämper, M., Nielsen, S.G., 2004. The mass balance of dissolved thallium in the oceans. Mar. Chem. 85, 125–139. https://doi.org/10.1016/j.marchem.2003.09.006

Rudnick, R.L., Gao, S., 2003. 3.01 - Composition of the Continental Crust. Treatise on Geochemistry 1, 1–64. https://doi.org/http://dx.doi.org/10.1016/B0-08-043751-6/03016-4

Sorensen, J. V., Gueguen, B., Stewart, B.D., Peña, J., Rouxel, O., Toner, B.M., 2020. Large nickel isotope fractionation caused by surface complexation reactions with hexagonal birnessite. Chem. Geol. 119481. https://doi.org/10.1016/J.CHEMGEO.2020.119481

Spivak-Birndorf, L.J., Wang, S.J., Bish, D.L., Wasylenki, L.E., 2018. Nickel isotope fractionation during continental weathering. Chem. Geol. https://doi.org/10.1016/j.chemgeo.2017.11.028

Stumm, W., Morgan, J.J., 1996. Metal Ions in Aqueous Solutions: Aspects of Coordination Chemistry, in: Aquatic Chemistry: Chemical Equilibria and Rates in Natural Waters.

Takano, S., Liao, W.H., Tian, H.A., Huang, K.F., Ho, T.Y., Sohrin, Y., 2020. Sources of particulate Ni and Cu in the water column of the northern South China Sea: Evidence from elemental and isotope ratios in aerosols and sinking particles. Mar. Chem. 219, 103751. https://doi.org/10.1016/j.marchem.2020.103751

Takano, S., Tanimizu, M., Hirata, T., Shin, K.C., Fukami, Y., Suzuki, K., Sohrin, Y., 2017. A simple and rapid method for isotopic analysis of nickel, copper, and zinc in seawater using chelating extraction and anion exchange. Anal. Chim. Acta 967, 1–11. https://doi.org/10.1016/j.aca.2017.03.010

Tripathy, S.S., Kanungo, S.B., 2005. Adsorption of Co2+, Ni2+, Cu2+and Zn2+from 0.5 M NaCl and major ion sea water on a mixture of δ-MnO2and amorphous FeOOH. J. Colloid Interface Sci. 284, 30–38. https://doi.org/10.1016/j.jcis.2004.09.054

Twining, B.S., Baines, S.B., Vogt, S., Nelson, D.M., 2012. Role of diatoms in nickel biogeochemistry in the ocean. Global Biogeochem. Cycles 26, 1–9. https://doi.org/10.1029/2011GB004233

Vance, D., Little, S.H., Archer, C., Cameron, V., Andersen, M.B., Rijkenberg, M.J.A., Lyons, T.W., 2016. The oceanic budgets of nickel and zinc isotopes: the importance of sulfidic environments as illustrated by the Black Sea. Philos. Trans. R. Soc. A Math. Phys. Eng. Sci. 374, 20150294. https://doi.org/10.1098/rsta.2015.0294

Wang, R.M., Archer, C., Bowie, A.R., Vance, D., 2018. Zinc and nickel isotopes in seawater from the Indian Sector of the Southern Ocean: The impact of natural iron fertilization versus Southern Ocean hydrography and biogeochemistry. Chem. Geol. 1–13. https://doi.org/10.1016/j.chemgeo.2018.09.010

Wang, S.J., Rudnick, R.L., Gaschnig, R.M., Wang, H., Wasylenki, L.E., 2019. Methanogenesis sustained by sulfide weathering during the Great Oxidation Event. Nat. Geosci. 12. https://doi.org/10.1038/s41561-019-0320-z

Wang, S.J., Wasylenki, L.E., 2017. Experimental constraints on reconstruction of Archean seawater Ni isotopic composition from banded iron formations. Geochim. Cosmochim. Acta 206, 137–150. https://doi.org/10.1016/j.gca.2017.02.023

Wasylenki, L.E., Howe, H.D., Spivak-Birndorf, L.J., Bish, D.L., 2015. Ni isotope fractionation during sorption to ferrihydrite: Implications for Ni in banded iron formations. Chem. Geol. 400, 56–64. https://doi.org/10.1016/j.chemgeo.2015.02.007

Wegorzewski, A. V., Grangeon, S., Webb, S.M., Heller, C., Kuhn, T., 2020. Mineralogical transformations in polymetallic nodules and the change of Ni, Cu and Co crystal-chemistry upon burial in sediments.

Table 2. Mn-rich sediments analysed in this study and their Ni isotope compositions. Other sample details: depth in sediment, XRD (for MANOP) or identified MnOx phase (Mn nodules) selected elemental concentrations (for full list, see Table S2), Ni/Al ratios and Ni enrichment factors (where EF = $(\mathrm{Ni/Al})_{\mathrm{sample}} / (\mathrm{Ni/Al})_{\mathrm{UCC}}$).

	Depth (cm)	**XRD analysis?**	**Mn (wt%)**	**Fe (wt%)**	**P (wt%)**	**Al (wt%)**	**Ni (µg/g)**	**Ni/Al**	**Ni EF**	**δ^{60}Ni**	**2σ**
MANOP Site H sediments											
VULCAN 37BC MP8950 AAZ	3 - 4 cm	✓	4.77	4.08	0.14	5.27	872	0.017	54	-0.17	0.04
VULCAN 37BC MP5306 AAZ	5 - 7 cm		4.42	4.23	0.15	5.41	892	0.016	54	-0.18	0.05
Repeat										-0.24	0.03
VULCAN 37BC MP5307 AAZ	7 - 9 cm	✓	5.34	4.15	0.14	5.29	785	0.015	49	-0.21	0.04
VULCAN 37BC MP5310 AAZ	13 - 15 cm		2.12	3.75	0.13	4.80	379	0.008	26	-0.27	0.05
VULCAN 37BC MP5312 AAZ	17 - 19 cm		2.12	3.99	0.15	5.17	382	0.007	24	-0.29	0.06
Repeat										-0.28	0.05
VULCAN 37BC MP5313 AAZ	19 -21 cm	✓	2.09	3.99	0.15	5.26	379	0.007	24	-0.26	0.03
MANOP Site M sediments											
PLUTO 20BC MP8966 AAZ	0.5 - 1 cm		1.43	5.45	0.12	4.16	286	0.007	23	-0.42	0.04
PLUTO 20BC MP8967 AAZ	1 - 3 cm	✓	1.65	5.92	0.13	4.69	317	0.007	22	-0.46	0.04
PLUTO 20BC MP8969 AAZ	5 - 7 cm		1.27	5.30	0.12	4.19	256	0.006	20	-0.43	0.04
PLUTO 20BC MP8971 AAZ	9 - 11 cm		0.85	5.40	0.11	4.23	228	0.005	18	-0.63	0.04
PLUTO 20BC MP8975 AAZ	17 - 19 cm		0.12	5.35	0.09	4.11	229	0.006	18	-0.79	0.05
Mn Nodules	**Depth (cm)**	**Main MnOx phase**									
USGS NodA1	Surface	Phyllomanganates	19.8	9.75	0.45	1.63	5732	0.352	1153	1.06	0.02^{*}
USGS NodP1	Surface	Phyllomanganates	30.1	4.91	0.16	1.36	11559	0.850	2784	0.34	0.05^{*}
21KG-1n	Surface	Phyllomanganates	31.6	4.29	0.11	1.57	11000	0.790	2587	0.28	0.03
77BC-6	Shallow buried	Todorokite	48.2	0.62	0.05	0.67	1884	0.793	2599	-0.22	0.04
22KL-530cm	Buried, 530cm	Todorokite	31.7	3.23	0.09	1.83	10328	0.452	1482	-0.08	0.04
22KL-801cm	Buried, 801cm	Todorokite	31.9	3.37	0.09	2.03	11492	0.351	1150	0.01	0.03

*n = 5, 2 SD

Supplementary information containing:

1. Ni column chemistry procedures
2. Mineralogy of MANOP samples by XRD (Table S1, Figs S1-S4)
3. Organic C hosted delivery of Ni to MANOP sediments (Fig S5)
4. The oceanic mass balance of Ni: Monte Carlo simulation (Figs S6-S8)

Supplementary Information for "Towards balancing the oceanic Ni budget"

S.H. Little et al., 2020

1. Ni column chemistry procedures

The methods used in this study to isolate Ni from its interfering matrix elements have been built upon previous methods used in this lab, and are described in detail elsewhere (Cameron et al., 2009; Ciscato et al., 2018; Vance et al., 2016; Wang et al., 2018). However during this work, the methodology used to purify Ni was changed from the Ni-specific (Eichrom) DMG based resin protocols as described in the earlier work (Cameron et al., 2009; Ciscato et al., 2018; Vance et al., 2016) to a modification of the multi-step protocol described in Wang et al. (2018) (Fig. 2, main text). The main advantage to adopting the multi-step protocol was a reduction of the procedural blank, from an amount as high as 5 ng to negligible values (Archer et al., 2020; Cameron et al., 2009). However, as alluded to by Archer et al. (2020), although the Nobias PA-1 chelate resin produces a matrix-free Ni fraction for seawater samples, the large amounts of Al and Ti that co-exist as potentially interfering matrix elements in sediments or rocks are not removed. Two additional columns were employed to quantitatively remove these elements (Fig. 2). Firstly, the Ni fraction was passed through a cation exchange resin (AG 50W X8, Bio-Rad Inc.) to remove any Al, with Ni eluted in a 0.75 M HCl solution. Secondly, Ti was removed by passing the Al-cleaned Ni fraction through the rare earth specific "Re-Resin" (Eichrom), with Ni eluted in a 7M HCl solution. Both of these columns provide quantitative recovery and separation of Ni from Al and Ti respectively with negligible blank contribution, with the interfering element retained on the resin in both cases. To remove any residual organics, the pure Ni fraction was oxidised by refluxing in a mixture of 15M HNO_3 and H_2O_2 for approximately 1 hour, before finally dissolving in a 2% HNO_3 solution for mass spectrometric analysis.

2. Mineralogy of MANOP samples by XRD

Samples were homogenized in an agate pestle and mortar and then back-loaded into 16mm internal diameter stainless steel sample holders. A PANalytical X'Pert PRO XRD instrument was used to collect X-ray powder diffraction patterns between 4 and 90° 2θ at a step size of 0.02° and a collection time of 400 or 800 second per step. The operation conditions for the Cu radiation source were 45 kV and 40 mA, and a Ni filter was used to remove Cu Kβ radiation.

Diffraction patterns were initially interpreted using the Highscore software (PANalytical) with the PDF-2 database from ICDD. Phase quantification was subsequently attempted via a Rietveld refinement analysis of the 10 – 90° 2θ region using BGMN-Profex (Bergmann et al., 1998; Doebelin and Kleeberg, 2015). Crystal structure data for the identified phases were taken from the ICSD and BGMN databases. The major phase smectite was refined with the turbostratically disordered structure model developed by Ufer et al. (2004). The plagioclase structure was refined with an andesine model. The fitting of the diffraction patterns included the refinement of the global parameters background (Lagrange polynomial 7th-8th order) and sample displacement, and the phase parameters scale factors, unit cells, peak profiles and preferred orientation. Refined texture correction factors converged in the range between 0.5 and 3, which is the proposed range for slightly textured samples (e.g., Monecke et al., 2001). The refinements were carried out between 10 and 90º 2θ excluding the broad region of the low-intense basal 001-reflection of smectite (4-8º 2Theta). This 001-reflection of smectite is poorly defined under air dried conditions (1 and/or 2 water interlayers contribute to peak shifts), can affect proper fitting of the background curve and inclusion in the refinement can lead to unclear results (Ufer et al., 2004). The results of the Rietveld analysis are shown in Figures S1 to S4 and Table S1.

The bulk mineral assemblages of the four MANOP samples are similar. The major mineral phase in all samples is smectite (49 – 60 wt%). The broad asymmetric band 02,11 between 19 and 26° 2θ indicates the occurrence of a dioctahedral clay species (montmorillonite) with a turbostratic disordered structure. Other minerals present in all samples include calcite (0.1 – 22 wt%), plagioclase (13 – 20 wt%), quartz (4 – 6 wt%), halite (4 – 5 wt%), kaolinite (4 – 6 wt%) and barite (1 – 3 wt%). A Mn oxide phase, tentatively identified as birnessite, is present at levels close to the detection limit of the XRD analysis (0.3 – 2 wt%). Muscovite (4 wt%) is identified in the sample from site M (8967, 1–3 cm depth) only, representing the only notable difference between this sample and the deepest sample at site H (5313, 19–21 cm), which are otherwise similar in their phase quantification. Both have significant calcite (at ~20 wt%), considerably more than the two shallower samples from site H (8950, at 3–4 cm, and 5307, at 7–9 cm), which contain 0.1 and 5 wt% calcite respectively. These two shallower site H samples, however, contain proportionally more smectite (at ~60 wt%) and larger amounts of the postulated Mn oxide phase (at ~ 1 wt%) than the site M and deeper site H samples (i.e. 5313 and 8967).

Table S1. XRD: Phase proportions (wt%) of four MANOP samples derived from Rietveld analysis

			Site H				**Site M**	
	8950	+/-	**5307**	+/-	**5313**	+/-	**8967**	+/-
smectite	59.6	1.7	60.0	1.7	48.6	1.6	49.9	1.5
plagioclase	19.7	1.0	14.6	0.9	12.7	0.7	14.2	0.6
quartz	6.0	0.4	6.1	0.3	5.2	0.3	3.8	0.1
calcite	0.1	0.1	4.9	0.5	21.9	0.8	17.7	0.6
kaolinite	6.2	1.0	5.6	0.9	4.9	0.7	4.3	0.6
halite	4.5	0.3	5.1	0.3	4.6	0.2	3.9	0.2
barite	2.8	0.2	2.2	0.2	1.8	0.2	1.4	0.1
birnessite	1.1	0.2	1.5	0.2	0.3	0.1	0.3	0.1
muscovite	-	-	-	-	-	-	4.4	0.6
R_{wp} %	3.30		3.11		2.90		2.49	
R_{exp} %	2.00		2.05		1.56		1.43	
S	1.65		1.52		1.86		1.74	

Note: R_{wp} weighted residual error, R_{exp} expected error, S goodness of fit. Calculated uncertainties of phase proportions are given as 3 sigma

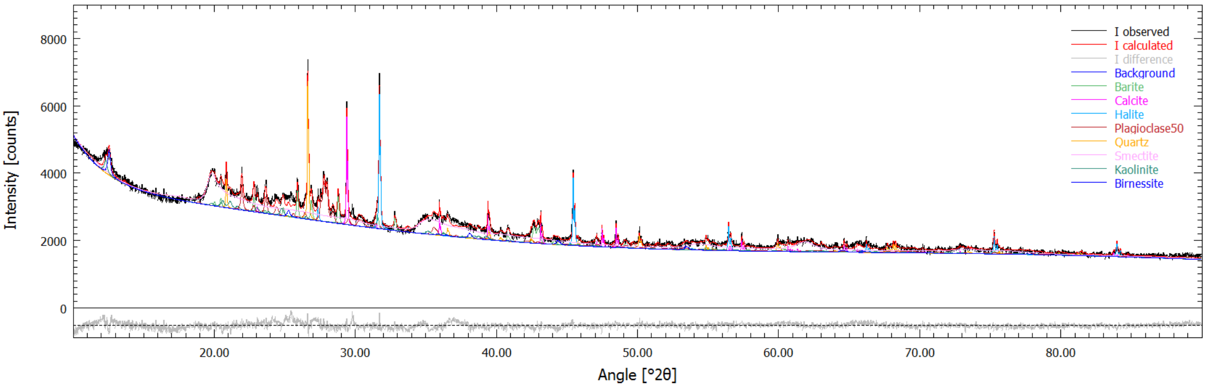

Figure S1. XRD pattern and Rietveld fit of MANOP sample 5307

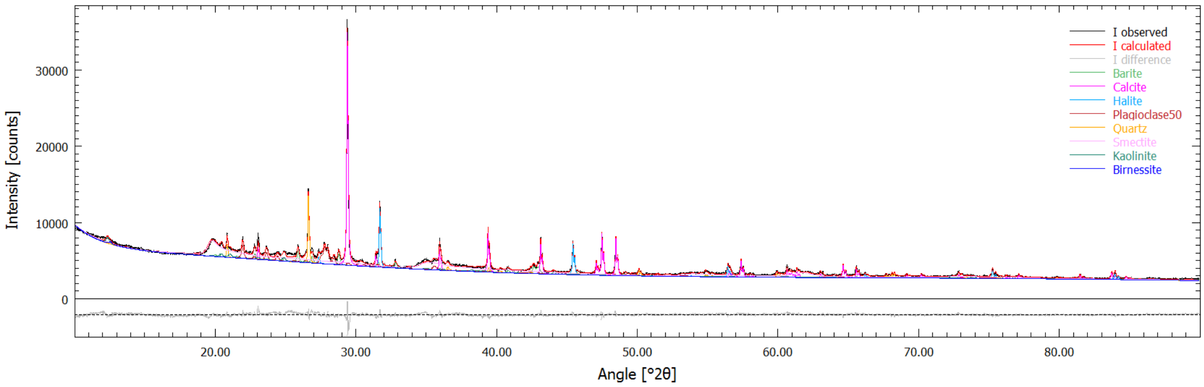

Figure S2. XRD pattern and Rietveld fit of MANOP sample 5313

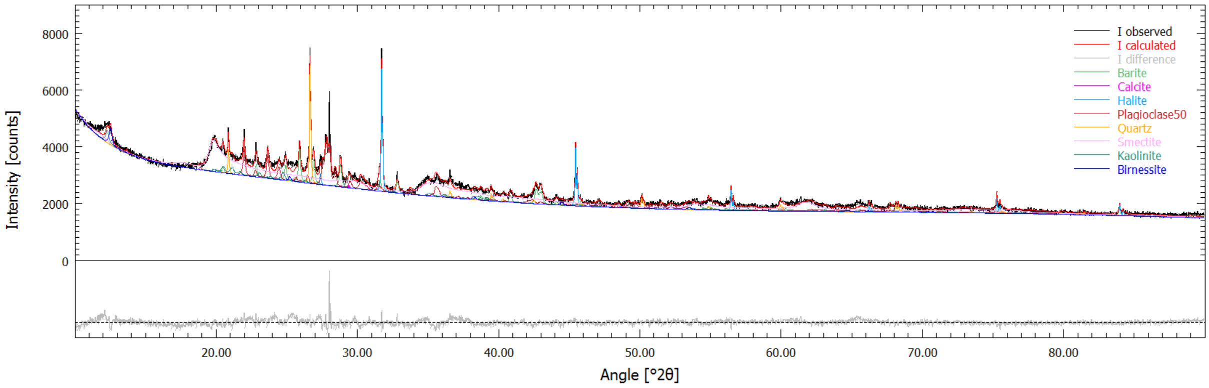

Figure S3. XRD pattern and Rietveld fit of MANOP sample 8950

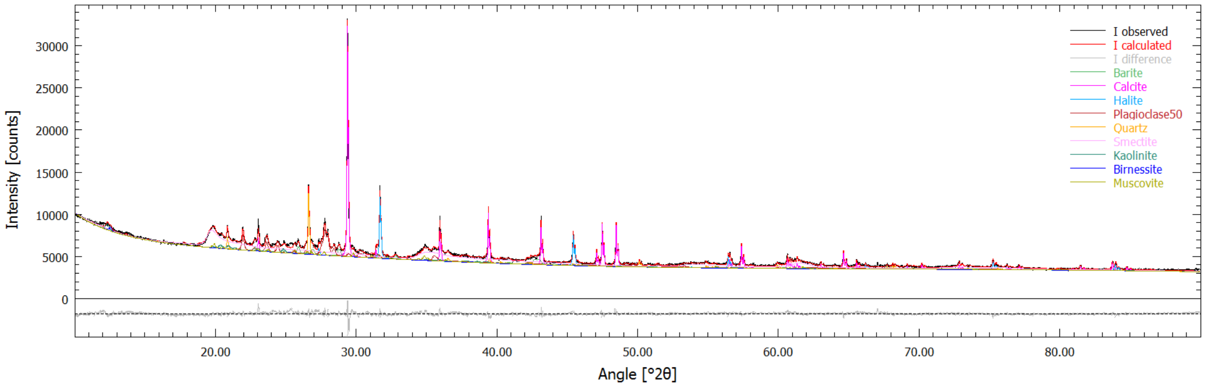

Figure S4. XRD pattern and Rietveld fit of MANOP sample 8967

3. Organic C hosted delivery of Ni to MANOP sediments

For calculation, please see separate Table S3.

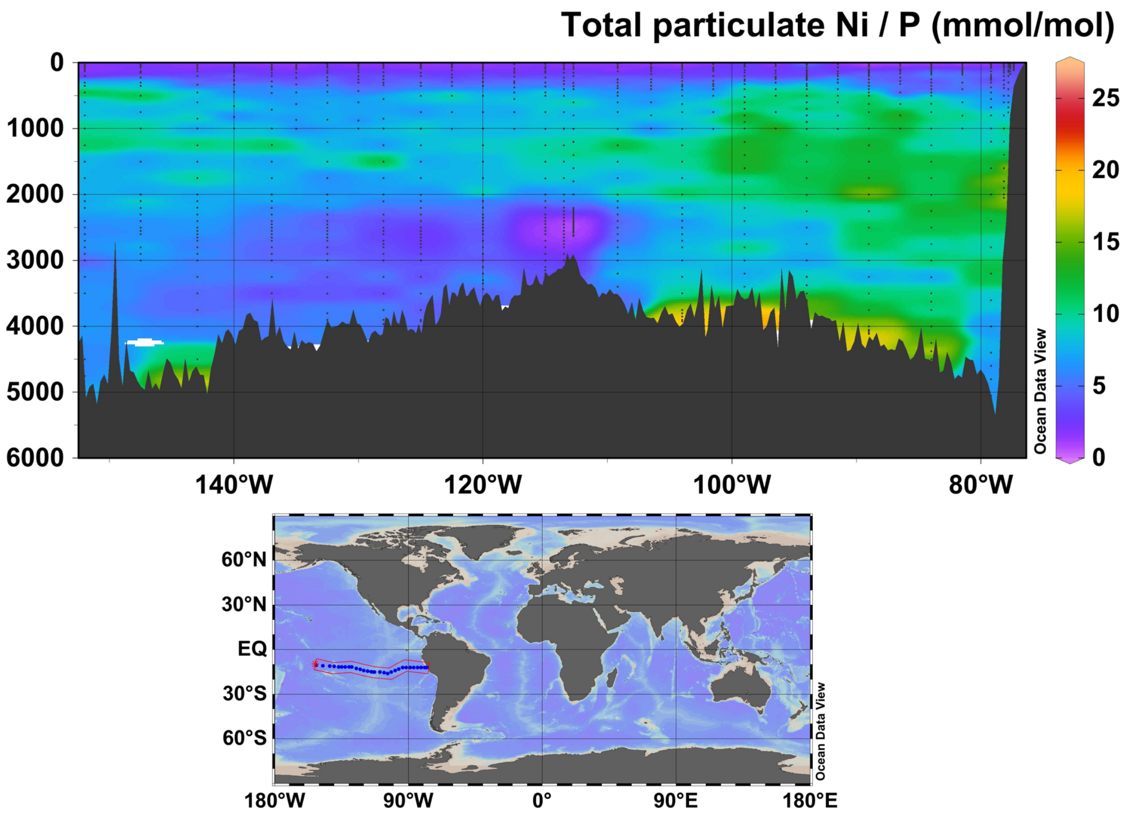

Figure S5. Total particulate Ni/P ratios (from bottle filtration) for GEOTRACES GP16 transect in the eastern equatorial Pacific (Dataset: Ohnemus et al., 2017). Plotted from the GEOTRACES IDP2017 (Schlitzer et al., 2018) using Ocean Data View software (Schlitzer, 2016).

4. The oceanic mass balance of Ni

The Monte Carlo simulation utilised the MATLAB solve tool, whereby two variables (e.g., $\delta^{60}Ni_{benthic}$, $F_{benthic}$) are solved for simultaneously given the following mass balance equations:

(1) $F_{river}\delta_{river} + F_{dust}\delta_{dust} + F_{benthic}\delta_{benthic} = F_{oxic}\delta_{oxic} + F_{org}\delta_{org} + F_{eux}\delta_{eux} + F_{carb}\delta_{carb}$

(2) $F_{river} + F_{dust} + F_{benthic} = F_{oxic} + F_{org} + F_{eux} + F_{carb}$

Prior to solving for the unknown variables (i.e. $\delta^{60}Ni_{benthic}$, $F_{benthic}$), the other flux magnitudes are forced by a uniformly distributed random number within their given ranges (Table 3, main text), and their isotopic compositions are forced by a normally distributed random number (see below), generating $\delta^{60}Ni$ values describing the mean and standard distribution of published data (Table 3, main text). With these initial conditions, the solve tool is then used to solve for the unknown variables, the output is saved, and the simulation is repeated (~10,000 times). Once the desired number of iterations is complete, the modelled benthic flux magnitude is restricted to its estimated range (as discussed in the main text) by discarding solutions outside of this range. This post-processing has the effect of reducing output flux range for pelagic clays to 1.6 – 4.6 x 10^8 mol/yr, compared to its starting range of 1.5 – 5.9 x 10^8 mol/yr. This result appears to be robust, however, emerging even if a different output flux variable is selected as an unknown (i.e. solving for F_{oxic} or F_{org} instead of $F_{benthic}$).

The decision to approximate the isotopic compositions of the 'known' output fluxes as normally distributed variables was made based on inspection and analysis of the published data for Fe-Mn crusts (Fig. S6A; Gall et al., 2013; Gueguen et al., 2016) and organic-rich sediments (Fig. S6B; Ciscato et al., 2018). The assumption of normality for a dataset is difficult to prove, but is supported if the following observations are made:

(1) Mean value similar to median value
(2) Skewness (measure of symmetry) between -2 and 2
(3) Kurtosis (measure of how quickly data tails off) between -2 and 2
(4) 'Normal' looking distribution when plotted as a histogram

All four criteria are met for both datasets, albeit that the number of datapoints are too small to be especially confident. This is particularly true for the organic-rich sediment dataset, which is from a single location (the Peru margin – see also below). Nevertheless, while imperfect, this approach was considered more appropriate than the uniformly-distributed approach taken for flux magnitudes.

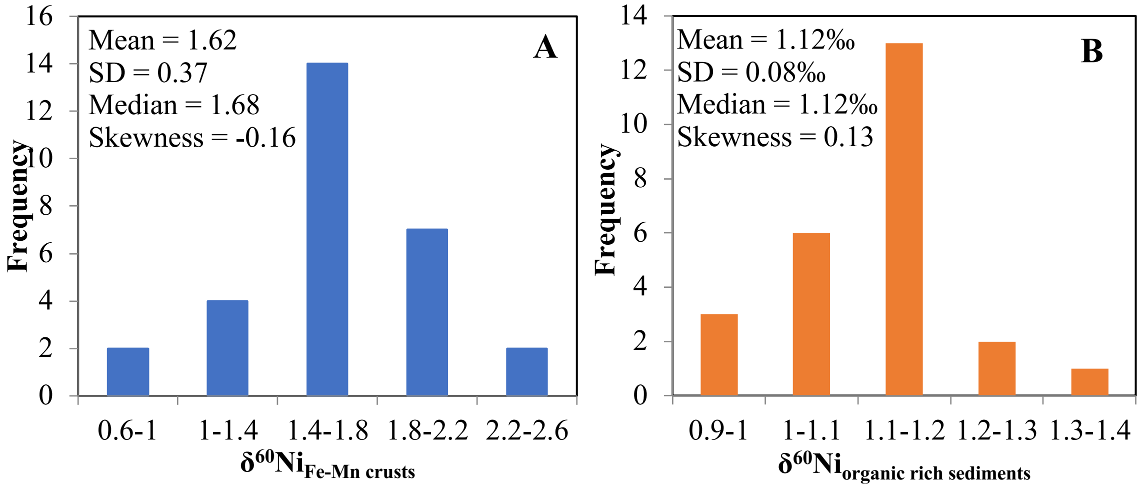

Figure S6. δ^{60}Ni datasets illustrated as frequency histograms showing 'normal'-like distributions, with selected descriptive statistics. **A.** Fe-Mn crusts (Gall et al., 2013, excluding one outlier at 0.43‰; and Gueguen et al., 2016, means) and **B.** organic-rich sediments (bulk digests, Ciscato et al., 2018).

Relatedly, our reanalysis of the dataset of Ciscato et al. (2018) gives a slightly lower mean $\delta^{60}Ni_{org}$ (of +1.12‰) and a slightly smaller upper limit to the flux to organic-rich sediments (of 2.4 x 10^8 mol/yr) than given in the original study (1.22‰ and 2.7 x 10^8 mol/yr, respectively). Our values are based on the bulk δ^{60}Ni and Ni/TOC ratios given in the original Table 2 (we exclude one anomalous bulk Ni/TOC ratio at 1.97 x 10^{-4}). We choose to cite bulk values (rather than corrected $\delta^{60}Ni_{auth}$ values) because there is a good correlation of TOC v Ni, with an intercept at ~0 µg/g Ni (Fig. S7), suggesting no major lithogenic Ni component. By comparison, there is significant scatter in a plot of TOC v Ni/Al, making it difficult to accurately constrain the lithogenic background Ni/Al ratio by this method (as originally suggested by Böning et al., 2012). In future, further studies of this important output flux will better constrain both its magnitude and isotopic composition.

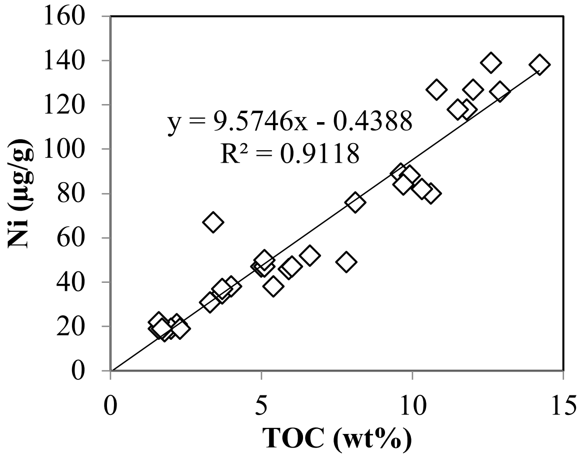

Figure S7. TOC versus Ni concentration for Peru margin organic-rich sediments (replotted from data in Ciscato et al., 2018).

Finally, the modelled isotopic composition on the benthic flux is visualised for the ~5000 ‘accepted’ solutions in Fig. S8. The distribution has a slight skew towards higher δ^{60}Ni; for this reason the median value is taken as the ‘best guess’ $\delta^{60}Ni_{benthic}$ value in Table 3 (main text). The range is given as the mean ± 1 SD.

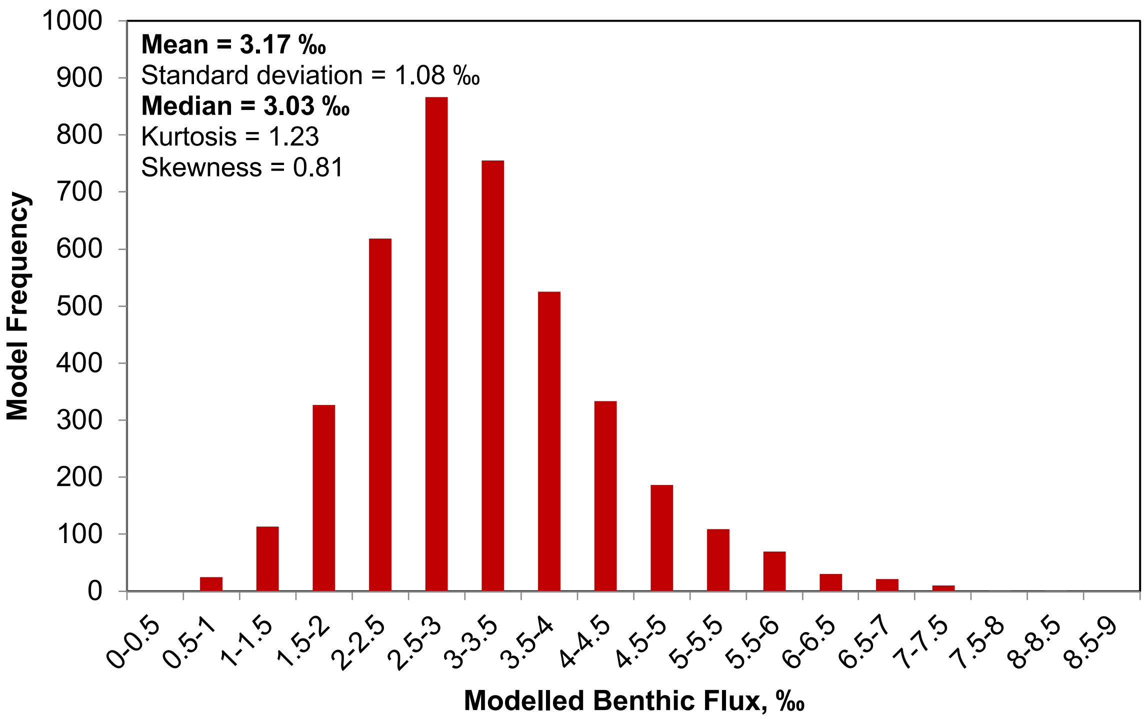

Figure S8. Histogram of the modelled $\delta^{60}Ni_{benthic}$, with selected descriptive statistics.

References

Archer, C., Vance, D., Lohan, M.C., Milne, A., 2020. The oceanic biogeochemistry of nickel and its isotopes: new data from the South Atlantic and the Southern Ocean biogeochemical divide. Earth Planet. Sci. Lett.

Bergmann, J., Friedel, P., Kleeberg, R., 1998. BGMN - a New Fundamental Parameters Based Rietveld Program for Laboratory X-ray Sources, it's Use in Quantitative Analysis and Structure Investigations. IUCr Comm. Powder Diffr. Newsl. 20, 5–8.

Böning, P., Fröllje, H., Beck, M., Schnetger, B., Brumsack, H.J., 2012. Underestimation of the authigenic fraction of Cu and Ni in organic-rich sediments. Mar. Geol. 323–325, 24–28. https://doi.org/10.1016/j.margeo.2012.07.004

Cameron, V., Vance, D., Archer, C., House, C.H., 2009. A biomarker based on the stable isotopes of nickel. Proc. Natl. Acad. Sci. 106, 10944–10948. https://doi.org/10.1073/pnas.0900726106

Ciscato, E.R., Bontognali, T.R.R., Vance, D., 2018. Nickel and its isotopes in organic-rich sediments: implications for oceanic budgets and a potential record of ancient seawater. Earth Planet. Sci. Lett. 494, 239–250. https://doi.org/10.1016/j.epsl.2018.04.061

Doebelin, N., Kleeberg, R., 2015. Profex: A graphical user interface for the Rietveld refinement program BGMN. J. Appl. Crystallogr. 48, 1573–1580. https://doi.org/10.1107/S1600576715014685

Gall, L., Williams, H.M., Siebert, C., Halliday, A.N., Herrington, R.J., Hein, J.R., 2013. Nickel isotopic compositions of ferromanganese crusts and the constancy of deep ocean inputs and continental weathering effects over the Cenozoic. Earth Planet. Sci. Lett. 375, 148–155. https://doi.org/10.1016/j.epsl.2013.05.019

Gueguen, B., Rouxel, O., Rouget, M.L., Bollinger, C., Ponzevera, E., Germain, Y., Fouquet, Y., 2016. Comparative geochemistry of four ferromanganese crusts from the Pacific Ocean and significance for the use of Ni isotopes as paleoceanographic tracers. Geochim. Cosmochim. Acta 189, 214–235. https://doi.org/10.1016/j.gca.2016.06.005

Monecke, T., Köhler, S., Kleeberg, R., Herzig, P.M., Gemmell, J.B., 2001. Quantitative phase-analysis by the Rietveld method using X-ray powder-diffraction data: Application to the study of alteration halos associated with volcanic-rock-hosted massive sulfide deposits. Can. Mineral. 39, 1617–1633. https://doi.org/10.2113/gscanmin.39.6.1617

Ohnemus, D.C., Rauschenberg, S., Cutter, G.A., Fitzsimmons, J.N., Sherrell, R.M., Twining, B.S., 2017. Elevated trace metal content of prokaryotic communities associated with marine oxygen deficient zones. Limnol. Oceanogr. 62, 3–25. https://doi.org/10.1002/lno.10363

Schlitzer, R., 2016. Ocean Data View.

Schlitzer, R., Anderson, R.F., Dodas, E.M., Lohan, M., Geibert, W., Tagliabue, A., Bowie, A., Jeandel, C., Maldonado, M.T., Landing, W.M., Cockwell, D., Abadie, C., Abouchami, W., Achterberg, E.P., Agather, A., Aguliar-Islas, A., van Aken, H.M., Andersen, M., Archer, C., Auro, M., de Baar, H.J., Baars, O., Baker, A.R., Bakker, K., Basak, C., Baskaran, M., Bates, N.R., Bauch, D., van Beek, P., Behrens, M.K., Black, E., Bluhm, K., Bopp, L., Bouman, H., Bowman, K., Bown, J., Boyd, P., Boye, M., Boyle, E.A., Branellec, P., Bridgestock, L., Brissebrat, G., Browning, T., Bruland, K.W., Brumsack, H.-J., Brzezinski, M., Buck, C.S., Buck, K.N., Buesseler, K., Bull, A., Butler, E., Cai, P., Mor, P.C., Cardinal, D., Carlson, C., Carrasco, G., Casacuberta, N., Casciotti, K.L., Castrillejo, M., Chamizo, E., Chance, R., Charette, M.A., Chaves, J.E., Cheng, H., Chever, F., Christl, M., Church, T.M., Closset, I., Colman, A., Conway, T.M., Cossa, D., Croot, P., Cullen, J.T., Cutter, G.A., Daniels, C., Dehairs, F., Deng, F., Dieu, H.T., Duggan, B., Dulaquais, G., Dumousseaud, C., Echegoyen-Sanz, Y., Edwards, R.L., Ellwood, M., Fahrbach, E., Fitzsimmons, J.N., Russell Flegal, A., Fleisher, M.Q., van de Flierdt, T., Frank, M., Friedrich, J., Fripiat, F., Fröllje, H., Galer, S.J.G., Gamo, T., Ganeshram, R.S., Garcia-Orellana, J., Garcia-Solsona, E., Gault-Ringold, M., George, E., Gerringa, L.J.A., Gilbert, M., Godoy, J.M., Goldstein, S.L., Gonzalez, S.R., Grissom, K., Hammerschmidt, C., Hartman, A., Hassler, C.S., Hathorne, E.C., Hatta, M., Hawco, N., Hayes, C.T., Heimbürger, L.-E., Helgoe, J., Heller, M., Henderson, G.M., Henderson, P.B., van Heuven, S., Ho, P., Horner, T.J., Hsieh, Y.-T., Huang, K.-F., Humphreys, M.P., Isshiki, K., Jacquot, J.E., Janssen, D.J., Jenkins, W.J., John, S., Jones, E.M., Jones, J.L., Kadko, D.C., Kayser, R., Kenna, T.C., Khondoker, R., Kim, T., Kipp, L., Klar, J.K., Klunder, M., Kretschmer, S., Kumamoto, Y., Laan, P., Labatut, M., Lacan, F., Lam, P.J., Lambelet, M., Lamborg, C.H., Le Moigne, F.A.C., Le Roy, E., Lechtenfeld, O.J., Lee, J.-M., Lherminier, P., Little, S., López-Lora, M., Lu, Y., Masque, P., Mawji, E., Mcclain, C.R., Measures, C., Mehic, S., Barraqueta, J.-L.M., van der Merwe, P., Middag, R., Mieruch, S., Milne, A., Minami, T., Moffett, J.W., Moncoiffe, G., Moore, W.S., Morris, P.J., Morton, P.L., Nakaguchi, Y., Nakayama, N., Niedermiller, J., Nishioka, J., Nishiuchi, A., Noble, A., Obata, H., Ober, S., Ohnemus, D.C., van Ooijen, J., O’Sullivan, J., Owens, S., Pahnke, K., Paul, M., Pavia, F., Pena, L.D., Peters, B., Planchon, F., Planquette, H., Pradoux, C., Puigcorbé, V., Quay, P., Queroue, F., Radic, A., Rauschenberg, S., Rehkämper, M., Rember, R., Remenyi, T., Resing, J.A., Rickli, J., Rigaud, S., Rijkenberg, M.J.A., Rintoul, S., Robinson, L.F., Roca-Martí, M., Rodellas, V., Roeske, T., Rolison, J.M., Rosenberg, M., Roshan, S., Rutgers van der Loeff, M.M., Ryabenko, E., Saito, M.A., Salt, L.A., Sanial, V., Sarthou, G., Schallenberg, C., Schauer, U., Scher, H., Schlosser, C., Schnetger, B., Scott, P., Sedwick, P.N., Semiletov, I., Shelley, R., Sherrell, R.M., Shiller, A.M., Sigman, D.M., Singh, S.K., Slagter, H.A., Slater, E., Smethie, W.M., Snaith, H., Sohrin, Y., Sohst, B., Sonke, J.E., Speich, S., Steinfeldt, R., Stewart, G., Stichel, T., Stirling, C.H., Stutsman, J., Swarr, G.J., Swift, J.H., Thomas, A., Thorne, K., Till, C.P., Till, R., Townsend, A.T., Townsend, E., Tuerena, R., Twining, B.S., Vance, D., Velazquez, S., Venchiarutti, C., Villa-Alfageme, M., Vivancos, S.M., Voelker, A.H.L., Wake, B., Warner, M.J., Watson, R., van Weerlee, E., Alexandra Weigand, M., Weinstein, Y., Weiss, D., Wisotzki, A., Woodward, E.M.S., Wu, J., Wu, Y., Wuttig, K., Wyatt, N., Xiang, Y., Xie, R.C., Xue, Z., Yoshikawa, H., Zhang, J., Zhang, P., Zhao, Y., Zheng, L., Zheng, X.-Y., Zieringer, M., Zimmer, L.A., Ziveri, P., Zunino, P., Zurbrick, C., 2018. The GEOTRACES Intermediate Data Product 2017. Chem. Geol. https://doi.org/10.1016/j.chemgeo.2018.05.040

Ufer, K., Georg, R., Reinhard, K., Helge, S., Reiner, D., Jörg, B., 2004. Description of X-ray powder pattern of turbostratically disordered layer structures with a Rietveld compatible approach. Zeitschrift für Krist. - Cryst. Mater. 219, 519–527. https://doi.org/10.1524/zkri.219.9.519.44039

Vance, D., Little, S.H., Archer, C., Cameron, V., Andersen, M.B., Rijkenberg, M.J.A., Lyons, T.W., 2016. The oceanic budgets of nickel and zinc isotopes: the importance of sulfidic environments as illustrated by the Black Sea. Philos. Trans. R. Soc. A Math. Phys. Eng. Sci. 374, 20150294. https://doi.org/10.1098/rsta.2015.0294

Wang, R.M., Archer, C., Bowie, A.R., Vance, D., 2018. Zinc and nickel isotopes in seawater from the Indian Sector of the Southern Ocean: The impact of natural iron fertilization versus Southern Ocean hydrography and biogeochemistry. Chem. Geol. 1–13. https://doi.org/10.1016/j.chemgeo.2018.09.010

Supplementary Table S2

			Elemental concentrations	
MANOP Site H sediments	**Depth (cm)**	**XRD?**	**Mn (wt%)**	**Fe (wt%)**
VULCAN 37BC MP8950 AAZ	3 - 4 cm	x	4.77	4.08
VULCAN 37BC MP5306 AAZ	5 - 7 cm		4.42	4.23
VULCAN 37BC MP5307 AAZ	7 - 9 cm	x	5.34	4.15
VULCAN 37BC MP5310 AAZ	13 - 15 cm		2.12	3.75
VULCAN 37BC MP5312 AAZ	17 - 19 cm		2.12	3.99
VULCAN 37BC MP5313 AAZ	19 -21 cm	x	2.09	3.99
MANOP Site M sediments				
PLUTO 20BC MP8966 AAZ	0.5 - 1 cm		1.43	5.45
PLUTO 20BC MP8967 AAZ	1 - 3 cm	x	1.65	5.92
PLUTO 20BC MP8969 AAZ	5 - 7 cm		1.27	5.30
PLUTO 20BC MP8971 AAZ	9 - 11 cm		0.85	5.40
PLUTO 20BC MP8975 AAZ	17 - 19 cm		0.12	5.35
Mn Nodules	**Depth (cm)**	**Main MnOx**		
USGS NodA1	Surface	phyllomanganates	19.8	9.75
USGS NodP1	Surface	phyllomanganates	30.1	4.91
21KG-1n	Surface	phyllomanganates	31.6	4.29
77BC-6	Shallow buried	Todorokite	48.2	0.62
22KL-530cm	Buried, 530cm	Todorokite	31.7	3.23
22KL-801cm	Buried, 801cm	Todorokite	31.9	3.37

Mg (wt%)	Al (wt%)	P (wt%)	Ca (wt%)	Ti (wt%)	Li (µg/g)	Ni (µg/g)
1.36	5.27	0.14	1.25	0.25	65.4	872
1.41	5.41	0.15	1.71	0.31	49.6	892
1.39	5.29	0.14	2.79	0.30	32.8	785
1.20	4.80	0.13	8.31	0.28	28.6	379
1.26	5.17	0.15	7.25	0.29	31.6	382
1.27	5.26	0.15	7.50	0.29	32.5	379
1.34	4.16	0.12	6.10	0.22	33.7	286
1.52	4.69	0.13	6.55	0.24	37.7	317
1.37	4.19	0.12	6.32	0.21	26.7	256
1.39	4.23	0.11	9.26	0.21	29.9	228
1.53	4.11	0.09	11.45	0.21	32.1	229
2.78	1.63	0.45	10.52	0.25	65.8	5732
1.80	1.36	0.16	1.97	0.20	120.9	11559
1.74	1.57	0.11	1.32	0.19	179.2	12414
2.04	0.67	0.05	0.94	0.02	6.3	5313
2.14	1.83	0.09	0.86	0.11	22.3	8255
2.22	2.03	0.09	0.87	0.10	20.1	7109

			Selected ratios		
Cu (µg/g)	Zn (µg/g)	Mo (µg/g)	Fe/Al	Ni/Mn	Ni/P mmol/mc
512	537	39.1	0.78	0.018	319
523	492	59.6	0.78	0.020	305
481	400	34.9	0.78	0.015	289
354	316	5.5	0.78	0.018	150
387	343	5.5	0.77	0.018	139
388	347	5.4	0.76	0.018	135
193	307	9.9	1.31	0.020	128
217	341	11.4	1.26	0.019	127
188	298	4.0	1.26	0.020	116
195	301	1.7	1.28	0.027	109
142	317	0.4	1.30	0.187	131
1017	541	326	5.98	0.029	676
10190	1363	535	3.61	0.038	3916
11000	1615	601.6	2.73	0.039	5817
1884	952	275.6	0.93	0.011	5581
10328	617	195.9	1.77	0.026	4832
11492	602	151.4	1.66	0.022	4356

ol

Table S3: Calculated delivery of Ni to MANOP sediments via sinking organic matter

Eq. Pacific plankton Ni/P	g Ni / g P	Bulk plankton	1.08 mmol/mol	0.0020
Twining et al., 2012		SD	0.41 mmol/mol	0.0008
		min	0.25 mmol/mol	0.0005
		max	1.15 mmol/mol	0.0022

Particulate Ni/P along GP16, below mixed layer	Range, upper	15 mmol/mol	0.0284
Ohnemus et al., 2017 (Fig. S5)	Range, lower	5 mmol/mol	0.0095

			Site H	Site M
Corg flux	µg / cm^{2}yr		110	130
Calculated org P flux	µg / cm^{2}yr		2.3	2.7
Calculated org Ni flux				
Plankton Ni/P	µg / cm2yr	Bulk plankton	0.0047	0.0055
		SD	0.0018	0.0021
		min plankton	0.0011	0.0013
		max plankton	0.0050	0.0059
Particulate Ni/P	µg / cm2yr	Upper Ni/P_{part}	0.0651	0.0769
		Lower Ni/P_{part}	0.0217	0.0256
Density	g / cm^3		0.168	0.211
g dry, salt-free sediment/cm3 wet sediment			0.212	0.255
Sedimentation Rate	cm / yr		0.0007	0.001
Mass accumulation rate	g / cm2yr		0.000148	0.000255
Calculated Ni concentration supplied by organic matter	µg/g	Bulk plankton	32	22
		min plankton	7	5
		max plankton	34	23
		Upper Ni/P_{part}	439	301
		Lower Ni/P_{part}	146	100
Measured Ni concentration *Whole cores*	µg / g	min	379	229
		max	892	317
		mean	615	263
		median	584	256
Ni concentration supplied by organic matter	% of mean Ni	Bulk plankton	5	8
		min plankton	1	2
		max plankton	5	9

Upper Ni/P_{part}	71	114
Lower Ni/P_{part}	24	38

References

Lyle, M., Heath, G.R., Robbins, J.M., 1984. Transport and release of transition elements during earl
Cochran, J. K. (1985). Particle mixing rates in sediments of the eastern equatorial Pacific: Evidence
Kadko, D.C., 1981. A detailed study of uranium-series nuctides for several sediment regimes of the
Ohnemus, D.C., Rauschenberg, S., Cutter, G.A., Fitzsimmons, J.N., Sherrell, R.M., Twining, B.S., 201
Twining, B.S., Baines, S.B., Vogt, S., Nelson, D.M., 2012. Role of diatoms in nickel biogeochemistry

g Ni / g P		
g Ni / g P		
g Ni / g P		
g Ni / g P		

	A.W.	Redfield		
C	12	124	1488	48.05
P	30.97	1	30.97	

g Ni / g P
g Ni / g P

	Reference, notes	
	Lyle et al., 1984	
	Assumes atomic C:P ratio of 124:1	
	Cochrane, 1985	*Average: upper 5 cm of one core and one lander char*
		Average: upper 19 cm, one core each site
	Kadko, 1981 (thesis, by 230Th and 231Pa)	

y diagenesis: Sequential leaching of sediments from MANOP Sites M and H. Part I. pH 5 aceti
from 210Pb, 239,240 Pu and 137Cs distributions at MANOP sites. *Geochimica et Cosmochimic*
Pacific. Columbia University.
.7. Elevated trace metal content of prokaryotic communities associated with marine oxygen d
in the ocean. Global Biogeochem. Cycles 26, 1–9. https://doi.org/10.1029/2011GB004233

nber at each site

---

c acid leach. *Geochim. Cosmochim. Acta 48* , 1705–1715.
a Acta , *49* (5), 1195-1210.

eficient zones. Limnol. Oceanogr. 62, 3–25. https://doi.org/10.1002/lno.10363